Lehrstuhl für Hochfrequenztechnik
der Technischen Universität München

Transmission Line Matrix – Multipole Expansion Method

Petr Lorenz

Vollständiger Abdruck der von der Fakultät für Elektrotechnik und Informationstechnik der Technischen Universität München zur Erlangung des akademischen Grades eines

Doktor-Ingenieurs

genehmigten Dissertation.

Vorsitzender: Univ.-Prof. Paolo Lugli, Ph.D.

Prüfer der Dissertation:

1. Univ.-Prof. Dr. techn. Peter Russer
2. Prof. Dr. Wolfgang J. R. Hoefer
   University of Victoria/Kanada

Die Dissertation wurde am 20.02.2007 bei der Technischen Universität München eingereicht und durch die Fakultät für Elektrotechnik und Informationstechnik am 02.07.2007 angenommen.

Transmission Line Matrix – Multipole Expansion Method

Petr Lorenz

Institute for High-Frequency Engineering
at the Technische Universität München

For my wife
and my parents

Acknowledgements

First of all, I would like to thank to my “Doktorvater” Prof. Dr. techn. Peter Russer for giving me the opportunity to work on such interesting and challenging topic at the Institute for High-Frequency Engineering, and for his time spent during for me so precious discussions. Thanks to him I could learn and enjoy the scientific life, even in the not so easy days of today’s science.

I want also to thank to my colleagues at the Institute and all the students with whom I have spent many hours by discussing the topic.

In my private life I can not thank enough to my wife Ivana for her support, patience, tolerance, those many weekends I have spent working on the topic and her love.

Furthermore, I want to thank to my parents and my grandmother for making it possible for me to get to know Germany and for encouraging and supporting me in my academic education. Also, many thanks go to all the others of the family and friends who were always supporting me in my work.

Lenggries, February 2007

Abstract

In this thesis the Transmission Line Matrix — Multipole Expansion method (TLMME) is presented. The TLMME method allows an efficient and potentially exact modeling of radiating electromagnetic structures. In the TLMME the time-domain Transmission Line Matrix (TLM) method is combined with the multipole expansion (ME) method of the radiated field.

The total radiated field is decomposed into orthonormal radiation modes which are connected to the TLM simulation domain on a common spherical boundary. In a global network model the simulation domain is modeled by the TLM mesh of transmission lines, every impedance of the radiation mode is modeled by a ladder network one port and the connection of these partial networks is accomplished by a connection subnetwork consisting of ideal transformers. This allows to include potentially exact radiating boundary condition into the TLM model by lumped element equivalent circuits representing the impedances of radiation modes.

Contents

1 Introduction and Overview

We live in time where the demand for electronic devices, electronic instruments, electronic systems and electronic information processing devices is booming. Not only became these devices indispensable tools in everyday life but our society became dependent on them. To name just a few examples: it is "impossible" to imagine air traffic control without radio communication, medical surgery without an electrocardiograph (ECG), information processing without an electronic computer or information spreading without the Internet.

The underlying fabric of all these devices and systems are electric charges and with them associated electromagnetic fields. It is thus no wonder that there is a high demand for tools which let us better understand, optimize, design and synthesize electronic devices and systems. Numerical methods for electromagnetics are such tools. With them we obtain an approximative solution of the electromagnetic equations.

The physical model of electromagnetic phenomena has been completed by James Clerk Maxwell in the year 1865 in his paper "A Dynamical Theory of the Electromagnetic Field". The four electromagnetic equations are called in honour of Maxwell's work Maxwell's equations. In his work Maxwell has introduced the displacement current $\mathcal{J}_D$,

$$\mathcal{J}_D = \frac{\partial \mathcal{D}}{\partial t}$$

as a temporal rate of change of the electric flux density $\mathcal{D}$. The displacement current has established a coupling between the electric and the magnetic field.

However, even if the theory of electromagnetism is 142 years old now[1],

[1] In 2007.

the solutions of the equations of electromagnetic field can be found analytically for a very limited set of problems. Actually, most of technically interesting problems do not have an analytic solution, or we do not know how to find it. In these cases we seek for an approximate solution using numerical methods.

Numerical methods and approximate solutions of electromagnetic equations have been gaining substantially on importance since about 40 years. The developments of powerful electronic computers in the last years have made it possible to solve numerically large problems at low cost. Today, full-wave[2] solutions of many technically interesting problems can be obtained using a personal computer (PC).

Special care must be taken if open radiating electromagnetic structures are to be characterized with a volumetric discretization method (more on the classification of numerical methods can be found in Section 1.2). This is so, because the computational resources are limited and we can create a numerical model for only a relatively small vicinity of the physical structure. The radiating properties are to be modeled by appropriate boundary conditions.

Numerical modeling of radiating boundary condition for the Transmission Line Matrix method is the focus of this thesis.

1.1 The Big Picture

In this thesis the Transmission Line Matrix (TLM) method is the numerical method of choice for one part of the spatial domain. Another part of the spatial domain is represented by multipole expansion (ME) technique. The two methods are combined using network oriented approach which is discussed in [1]. The matching of the electromagnetic field represented by TLM and ME can be seen as a mode matching technique.

The TLM method, as considered here, is a numerical time-domain technique which has been used since its introduction by Johns and Beurle [2] in 1971 to solve various problems in electromagnetic engineering [3]. In

[2] Full-wave solution is a solution for both, the electric and magnetic field, in space and time.

TLM the field is discretized in space and time and modeled by wave pulses propagating and being scattered in a mesh of transmission lines. When radiating electromagnetic structures are modeled the appropriate radiating boundary conditions at the boundary of the computational domain need to be included in the computation. In the literature methods to realize absorbing boundary conditions (ABCs) are discussed [4], [5], [6], [7], [8], [9]. These methods give approximate solutions of the problem by attenuating the radiating electromagnetic field, possibly without spurious reflections from the boundaries of the simulation domain.

On the other hand, the hybrid Transmision Line Matrix – Multipole Expansion (TLMME) method, which is described in this text, yields a potentially exact solution for general radiating electromagnetic structures in homogeneous media. In contrast to the ABC approach, the TLMME models the complete radiated field.

In this hybrid method the problem space is divided in two subspaces $\mathscr{R}_1$ and $\mathscr{R}_2$ connected at a common boundary $\mathscr{S}$ – see also Figure 1.1. Subspace $\mathscr{R}_1$ represents the TLM region where the discretized structure and the sources are modeled and subspace $\mathscr{R}_2$ represents the homogeneous background space where the radiating electromagnetic field is represented in terms of ME.

The connection between subspaces $\mathscr{R}_1$ and $\mathscr{R}_2$ is established from its network representation. The connection network, which connects subspace $\mathscr{R}_1$ and $\mathscr{R}_2$ and contains only ideal transformers [10], [1], is connected to lumped element equivalent circuits representing impedances of radiation modes.

The basis one-forms [11] of the ME are orthogonal and form a complete set. A compact lumped element LC ladder network representing the coupling between the electric and magnetic field intensities may be established [10].

In the TLM method the spherical boundary is approximated by cubical TLM cells. The connection of the outer faces of the TLM cells on the spherical boundary to the spherical modes is modeled by a connection subnetwork.

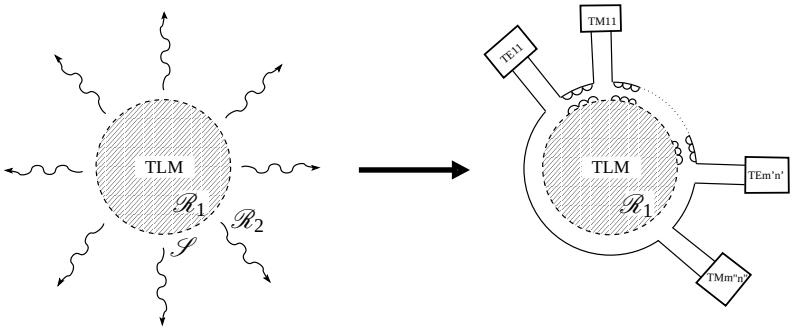

Figure 1.1: Left: schematic representation of the division of the unbounded space in subspaces $\mathscr{R}_1$ and $\mathscr{R}_2$ with the boundary $\mathscr{S}$. Right: schematic representation of the global network model of the TLMME simulation.

1.2 Numerical Solutions of Maxwell's Equations

In this Section a brief classification of main numerical methods used for solving the electromagnetic equations is given and the reason for the truncation of the simulation domain is shown.

For the numerical solution of Maxwell's equations various techniques have been proposed and new are still coming. We can distinguish between time-domain and frequency-domain techniques. Another possibility is to distinguish between volumetric discretization methods and surface discretization methods (see Figure 1.2). Volumetric discretization methods lead to finite-difference formulations, whereas surface discretization methods to integral equation formulations.

As we can see, there is a vast number of numerical methods one can use to solve the electromagnetic problem. However, not every method is suitable for a particular problem. A hybrid approach is an attractive way how to combine the power of different methods.

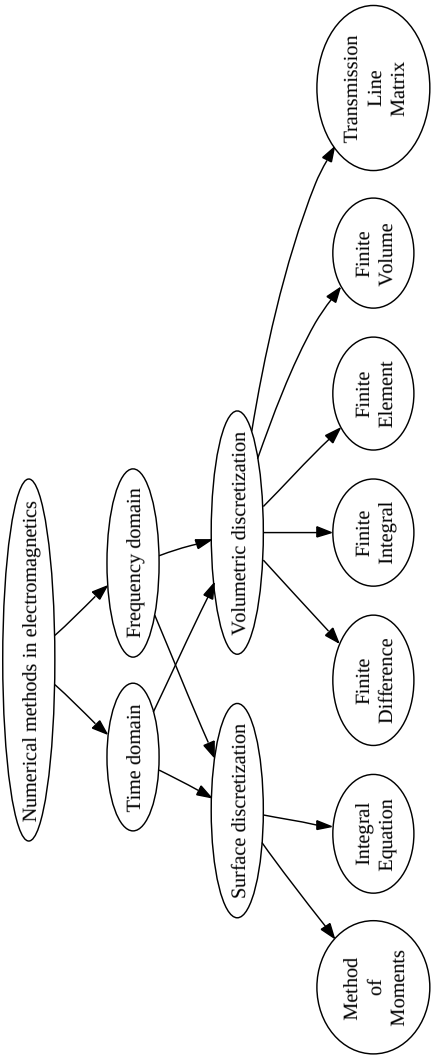

Figure 1.2: Classification of main numerical methods in electromagnetics.

Truncated simulation domains

Since the computational resources of today's computers are very limited, it is impossible to discretize large volumes of space. The limits up to which we are able to solve a problem are set by

- memory requirements,
- time needed to process the information.

To get a better feeling for what are the memory requirements to solve an electromagnetic problem, let us take a look at the following example. There is given a structure assumed to be perfect electric conductor (PEC) in air and we wish to compute the scattered electromagnetic field. A three-dimensional computational domain of $2000 \times 2000 \times 2000$ TLM cells requires $3\,072\,000\,000\,000$ bits[3] to hold the information about the electromagnetic field. This amount of information means

$$\frac{2000 \times 2000 \times 2000 \times 12 \times 32}{1024 \times 1024 \times 1024 \times 8} = 357.63\text{GB of memory.}$$

Increasing the spatial resolution just twice in every direction results in eight times larger memory requirements. For the particular example, 2 861GB of memory would be needed.

Consider that the human genome needs $70\,000\,000$ bits to hold its information. The previous example needs more than $40\,000$ times more. Furthermore, the time needed to process this amount of information is inverse proportional to the speed of information processing.

This example shows the reasons why we are not able to discretize very large structures. Consequently, the computational region must be truncated to finite, relatively small region around the physical structure. At the outer boundaries of this computational region special boundary conditions need to be applied.

[3] For the modeling of free-space we need 12 variables per TLM cell. We assume a TLM variable to be represented by a 32 bit floating point number.

For radiating structures the special boundary condition is called *radiating boundary condition*; for periodic structures *periodic boundary condition* is used; for resonating structures assumed to be inside a perfect electric conducting box *PEC boundary* conditions are applied; the dual perfect conducting magnetic walls *PMC boundary conditions* are used usually to impose symmetry conditions.

Of the mentioned boundary conditions the radiating boundary conditions are the most difficult ones to be realized numerically.

1.3 Organization of the Thesis

The thesis is organized as follows. In Chapter 2 the Transmission Line Matrix (TLM) method is described in detail. The principles of the method are shown from the point of view of statistical mechanics and the relation of the TLM scattering matrix to Maxwell's equations is expressed in terms of discrete differential forms. A way of modeling discrete sources suitable for the modeling of excitation of antenna structures is presented.

Chapter 3 is devoted to the multipole expansion (ME) method. The radiation modes and their canonical circuit realizations are described in detail.

Chapter 4 discusses the connection between the TLM domain and the outer domain represented in terms of ME. The fundamental Tellegen's theorem is described and the scattering matrix of the connection subnetwork is derived.

The hybridization of the TLM method and the ME method is presented in Chapter 5. First, the spherical TLM domain needed for the TLMME method is described in detail. Next, the pre-processing related tasks are discussed. The generation of the connection matrix and the realization of the canonical equivalent circuits of the radiation modes using wave digital filters (WDFs) are shown. The Chapter is concluded with the description of the TLMME algorithm.

Chapter 6 presents examples of electromagnetic solutions to antenna structures using the TLMME method and shows the validity, accuracy and new features of the method.

Finally, the conclusions of the thesis are presented in Chapter 7. Useful formulas, relations and operations are listed in Appendix A.

2 Transmission Line Matrix (TLM) Method

2.1 Principles of TLM

The Transmission Line Matrix (TLM) method is a discrete model, in space and time, of the electromagnetic phenomena.

The TLM method has been introduced by Johns in 1974 as a two dimensional method [12] and extended in 1987 for three dimensions with the development of symmetrical condensed node [13]. Since then there have been many attempts to derive the method directly from Maxwell's equations, and so to prove the validity of the method [14], [15], [16], [17], [18], [19].

The way from the continuous model to the discrete one is the standard way used to derive finite difference time domain (FDTD) method, finite integral technique (FIT) and other methods. Also, discrete differential calculus follows this way.

On the other hand, as Toffoli suggests (see [20] and [21]), the other way around, i.e., from a discrete model to the continuous one, is much more appropriate, if we want to develop intrinsically discrete models of nature. The argument, why we should do this, is supported by the rapid development of digital technologies and consequent information processing facilities. These make it possible to have new ways of describing the nature.

It is difficult, however, to cope with the idea of giving up the powerful techniques and models developed during the last 300 years represented by means of differential equations. The models have, however, their limits and most of technically interesting phenomena can not be solved by analytical techniques directly. But we do not want to give them up. We want to de-

velop alternative intrinsically discrete models of natural phenomena which will behave, under specific circumstances, like the analytical models.

The idea of a transition from a discrete description to a continuous one is well-known in statistical mechanics. In Section 2.2 we will see how the one-dimensional, two-dimensional and three-dimensional diffusion equations and the one-dimensional wave equation are obtained as continuum limits of intrinsically discrete models.

The TLM method can be seen in a broader view as a cellular automaton (CA). The notion of cellular automata has been first explored by John von Neumann. Cellular automata consist of independent computing units, which exchange their values with neighboring units and, accordingly, change their state. A cellular automaton has intrinsically parallel nature[1].

Usually, CA are considered to contain only discrete variables as their states. The Coupled Map Lattices (CML) [22] are computational models where the internal state of each cell is represented in terms of continuous variables, but space and time remain discrete. The computational mechanism of CML are identical with those of CA. Thus, the difference between CA and CML is in the representation of the state of a cell by a discrete or continuous variable, respectively[2].

The state of a TLM cell can be described by a vector of wave quantities. The transformation from one state to another – the computation of one cell – is represented by a scattering process. So, if the information about the state before scattering is stored in a vector **a** and the result of the scattering – computation – in a vector **b**, we may express the computation process of a TLM cell as

$$\mathbf{b} = \mathbf{S}\mathbf{a}, \tag{2.1}$$

where **S** is the scattering matrix. The scattering matrix defines the computation performed by a cell.

In a consequent step the information between neighboring cells is exchanged and the process starts from the beginning (more detailed descrip-

[1] With the introduction of multicore processors parallelism is gaining on importance more than ever.

[2] CML models have been used recently to implement physically-based visual simulations for real-time visual simulations [23].

tion of TLM iteration is given later in Section 5.3). This algorithm is equal to the algorithm of a cellular automaton using continuous state variables. In Section 2.3 it is shown how the TLM scattering matrices of two- and three-dimensional free-space TLM nodes can be obtained using discrete differential forms.

2.2 Statistical Mechanics, Diffusion Equation, and TLM

2.2.1 One-dimensional diffusion equation

In this Section it is shown how the behaviour of a discrete system in its continuum limit is investigated. In the text I follow the description and I use the same notation as in [24] (pp.15–20).

The one-dimensional diffusion equation is obtained as a continuum limit of one-dimensional uncorrelated random walk. A random walk is a process in which a particle moves a distance $|\pm\Delta x|$ in time Δt. The direction of the movement, i.e., in the positive or negative x-direction, is random. Both cases occur with the same probability.

We can describe the random walk by a probability distribution function $\chi(x)$ defined for the particular case of one-dimension as

$$\chi(x) = \frac{1}{2}\delta(x-\Delta x) + \frac{1}{2}\delta(x+\Delta x), \tag{2.2}$$

where $\delta(x)$ is the Dirac delta function. The first three moments of $\chi(x)$ are

$$\int \chi(x)\,\mathrm{d}x = 1, \tag{2.3a}$$

$$\int x\chi(x)\,\mathrm{d}x = 0, \tag{2.3b}$$

$$\int x^2\chi(x)\,\mathrm{d}x = (\Delta x)^2. \tag{2.3c}$$

We see from (2.3) that the mean value of $\chi(x)$ is zero and that the standard deviation is Δx.

The one-dimensional diffusion equation is given by the equation

$$\frac{\partial \rho(x,t)}{\partial t} = D\frac{\partial^2 \rho(x,t)}{\partial x^2}, \tag{2.4}$$

where D is the diffusion coefficient. The diffusion equation describes the evolution of the density function $\rho(x,t)$.

The density function $\rho(x,t)$ can be interpreted differently for a one particle system and a many particle system. For a one particle system the density function describes the evolution of the probability density for locating the particle at position x at time t. For many particle system the density function describes the density of diffunding particles (mass).

If we know the probability density $\rho(x,t)$ at a particular time t, its evolution at time $t+\Delta t$ can be written with (2.2) as

$$\rho(x,t+\Delta t) = \int \chi(x-x')\rho(x',t)\,\mathrm{d}x' = \int \chi(z)\rho(x-z,t)\,\mathrm{d}z, \tag{2.5}$$

with $z = x - x'$. Taking the Taylor expansion of $\rho(x-z,t)$ around x we can write (2.5) as

$$\rho(x,t+\Delta t) = \int \chi(z)\left[\rho(x,t) - z\frac{\partial \rho(x,t)}{\partial x} + \frac{z^2}{2}\frac{\partial^2 \rho(x,t)}{\partial x^2} + \ldots\right]\mathrm{d}z. \tag{2.6}$$

Using only the first three terms of the Taylor expansion in (2.6) we obtain with (2.3) the approximative expression

$$\rho(x,t+\Delta t) \approx \rho(x,t) + \frac{(\Delta x)^2}{2}\frac{\partial^2 \rho(x,t)}{\partial x^2}. \tag{2.7}$$

Reorganizing (2.7) and dividing both sides by Δt we obtain the approximative equation

$$\frac{1}{\Delta t}\Big(\rho(x,t+\Delta t) - \rho(x,t)\Big) \approx \frac{(\Delta x)^2}{2\Delta t}\frac{\partial^2 \rho(x,t)}{\partial x^2}. \tag{2.8}$$

In the continuum limit this equation becomes the diffusion equation (2.4) with the diffusion coefficient D given by

$$D = \frac{(\Delta x)^2}{2\Delta t}. \tag{2.9}$$

The random walk can be implemented numerically by an algorithm similar to the TLM algorithm (the CA algorithm). From (2.2) we know that if a particle arrives at time t at a node x_m, there is equal probability that at time $t+\Delta t$ this particle will be either at the node x_{m-1} or at the node x_{m+1}. The scattering matrix

$$\mathbf{S} = \frac{1}{2}\begin{bmatrix} 1 & 1 \\ 1 & 1 \end{bmatrix} \tag{2.10}$$

models then the one-dimensional diffusion equation.

2.2.2 Two- and three-dimensional diffusion equation

In a similar way to the previous Section we may derive the two-dimensional diffusion equation given by

$$\frac{\partial \rho(x,y,t)}{\partial t} = D\left(\frac{\partial^2 \rho(x,y,t)}{\partial x^2} + \frac{\partial^2 \rho(x,y,t)}{\partial y^2}\right). \tag{2.11}$$

The probability distribution for the two-dimensional random walk takes the form

$$\chi(x,y) = \frac{1}{4}\delta(x-\Delta x,y) + \frac{1}{4}\delta(x+\Delta x,y) + \frac{1}{4}\delta(x,y-\Delta y) + \frac{1}{4}\delta(x,y+\Delta y). \tag{2.12}$$

Using the two-dimensional Taylor expansion (see Appendix A, Equation (A.18)) it is possible to show that the two-dimensional random walk in its continuum limit corresponds to the two-dimensional diffusion equation.

Similarly to the one-dimensional case, the scattering matrix

$$\mathbf{S} = \frac{1}{4}\begin{bmatrix} 1 & 1 & 1 & 1 \\ 1 & 1 & 1 & 1 \\ 1 & 1 & 1 & 1 \\ 1 & 1 & 1 & 1 \end{bmatrix} \tag{2.13}$$

models the two-dimensional diffusion equation and the scattering matrix

$$\mathbf{S} = \frac{1}{6}\begin{bmatrix} 1 & 1 & 1 & 1 & 1 & 1 \\ 1 & 1 & 1 & 1 & 1 & 1 \\ 1 & 1 & 1 & 1 & 1 & 1 \\ 1 & 1 & 1 & 1 & 1 & 1 \\ 1 & 1 & 1 & 1 & 1 & 1 \\ 1 & 1 & 1 & 1 & 1 & 1 \end{bmatrix} \tag{2.14}$$

models the three-dimensional diffusion equation.

2.2.3 One-dimensional wave equation

The scattering matrix of the one-dimensional TLM method in free-space is given by

$$\mathbf{S} = \begin{bmatrix} 0 & 1 \\ 1 & 0 \end{bmatrix}. \tag{2.15}$$

We will see now that with this scattering matrix the one-dimensional wave equation is modeled. It is easy to check that the scattering matrix is energy conservative ($|\det(\mathbf{S})| = 1$) and invariant to time-reversal ($\mathbf{S} \cdot \mathbf{S} = \mathbf{I}$).

The one-dimensional wave equation is given by

$$\frac{\partial^2 \rho(x,t)}{\partial t^2} = c^2 \frac{\partial^2 \rho(x,t)}{\partial x^2}, \tag{2.16}$$

where the constant c is the speed of propagation.

Using the scattering matrix (2.15) the probability distribution function $\chi(x)$ can be written as

$$\chi(x) = \delta(x \pm \Delta x). \tag{2.17}$$

The first moments of the probability distribution are

$$\int \chi(x)\,\mathrm{d}x = 1, \tag{2.18a}$$

$$\int x\chi(x)\,\mathrm{d}x = \mp\Delta x, \tag{2.18b}$$

$$\int x^2\chi(x)\,\mathrm{d}x = (\Delta x)^2, \tag{2.18c}$$

$$\int x^3\chi(x)\,\mathrm{d}x = \mp(\Delta x)^3, \tag{2.18d}$$

$$\int x^4\chi(x)\,\mathrm{d}x = (\Delta x)^4, \tag{2.18e}$$

$$\vdots \tag{2.18f}$$

In analogy to (2.6) and by using (2.17) we get

$$\rho(x,t+\Delta t) = \int \chi(z)\rho(x-z,t)\,\mathrm{d}z = \int \rho(x-z,t)\,\delta(z\pm\Delta x)\,\mathrm{d}z = \rho(x\pm\Delta x,t) \tag{2.19}$$

which is the one-dimensional advection equation for the density function $\rho(x,t)$. In (2.19) we have used the sampling property of the Dirac delta function. From these two solutions we obtain directly the one-dimensional wave equation.

If we interpret the probability distribution $\rho(x,t)$ as wave quantities, we see from (2.19) that the wave quantities satisfy exactly

$$a(x,t+\Delta t) = a(x-\Delta x,t), \tag{2.20a}$$

$$b(x,t+\Delta t) = b(x+\Delta x,t). \tag{2.20b}$$

Using Taylor expansion we may approximate (2.20) by

$$a(x-\Delta x,t) = a(x,t) - \Delta x\frac{\partial a(x,t)}{\partial x} + O(\Delta x^2), \tag{2.21a}$$

$$b(x+\Delta x,t) = b(x,t) + \Delta x\frac{\partial b(x,t)}{\partial x} + O(\Delta x^2), \tag{2.21b}$$

which may be rewritten as (using approximations for smoothly varying quantities in space and time)

$$\frac{a(x,t+\Delta t)-a(x,t)}{\Delta t} \approx \frac{\partial a(x,t)}{\partial t} \approx -\frac{\Delta x}{\Delta t}\frac{\partial a(x,t)}{\partial x}, \tag{2.22a}$$

$$\frac{b(x,t+\Delta t)-b(x,t)}{\Delta t} \approx \frac{\partial b(x,t)}{\partial t} \approx \frac{\Delta x}{\Delta t}\frac{\partial b(x,t)}{\partial x}. \tag{2.22b}$$

These are the one-dimensional advection equations for the wave quantities $a(x,t)$ and $b(x,t)$.

Using the transformations (A.5b) from wave quantities to network quantities (see Appendix A) with $\eta = 1$ we have the following relations

$$V(x,t) = a(x,t) + b(x,t), \tag{2.23a}$$

$$I(x,t) = a(x,t) - b(x,t). \tag{2.23b}$$

Using (2.22) and (2.23) and defining $c = \frac{\Delta x}{\Delta t}$ we obtain the following equations for $V(x,t)$ and $I(x,t)$

$$\frac{\partial V(x,t)}{\partial x} = \frac{\partial a(x,t)}{\partial x} + \frac{\partial b(x,t)}{\partial x} = -\frac{1}{c}\left(\frac{\partial a(x,t)}{\partial t} - \frac{\partial b(x,t)}{\partial t}\right) = -\frac{1}{c}\frac{\partial I(x,t)}{\partial t}, \tag{2.24a}$$

$$\frac{\partial I(x,t)}{\partial x} = \frac{\partial a(x,t)}{\partial x} - \frac{\partial b(x,t)}{\partial x} = -\frac{1}{c}\left(\frac{\partial a(x,t)}{\partial t} + \frac{\partial b(x,t)}{\partial t}\right) = -\frac{1}{c}\frac{\partial V(x,t)}{\partial t}, \tag{2.24b}$$

which are the well-known Telegrapher's equations for voltage and current on a transmission line.

2.3 TLM Scattering Matrix in View of Discrete Differential Forms

The scattering matrix of the 2D TLM shunt node is equivalent to the scattering matrix of the parallel adaptor used in wave digital filters (WDFs)

[25]. In this section this equivalence is examined and it will be shown that also the 2D TLM scattering matrix with stubs can be obtained from the parallel adaptor of WDFs. The result can be generalized to obtain valid (by valid allowable is meant) TLM scattering matrices satisfying the following properties:

1. Frequency independent,
2. Invariant to time-reversal ($\mathbf{S} \cdot \mathbf{S} = \mathbf{I}$),
3. Energy conservative ($|\det(\mathbf{S})| = 1$),
4. Eigenvalues equal ± 1 (i.e., it is a connection matrix).

A standard 2D TLM shunt node is shown in Figure 2.1. The characteristic impedance of the link lines is $Z_0 = \sqrt{L/C}$. The interconnection at the center of the node will be called *cell center*. The cell center is delay-free, frequency independent and energy conservative. The scattering matrix of a shunt cell center equals to the scattering matrix of a parallel adaptor of WDF.

A 2D TLM cell center with a shunt stub line connection is shown in Figure 2.2. The reference impedances of the TLM link lines are $Z_0 = \frac{1}{Y_0}$ and the reference impedance of the stub line is $Z_s = \frac{1}{Y_s}$. The scattering matrix of parallel adaptor for the given cell center can be written as ([25], pp. 276–277)

$$\mathbf{S} = \begin{bmatrix} (\gamma-1) & \gamma & \gamma & \gamma & \gamma_s \\ \gamma & (\gamma-1) & \gamma & \gamma & \gamma_s \\ \gamma & \gamma & (\gamma-1) & \gamma & \gamma_s \\ \gamma & \gamma & \gamma & (\gamma-1) & \gamma_s \\ \gamma & \gamma & \gamma & \gamma & (\gamma_s-1) \end{bmatrix}, \tag{2.25a}$$

where

$$4\gamma + \gamma_s = 2 \quad \Rightarrow \quad \gamma_s = 2 - 4\gamma \tag{2.25b}$$

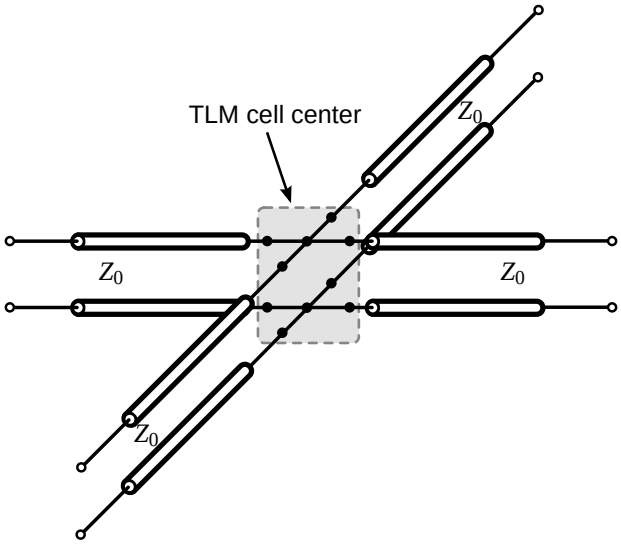

Figure 2.1: 2D TLM shunt node and its TLM cell center.

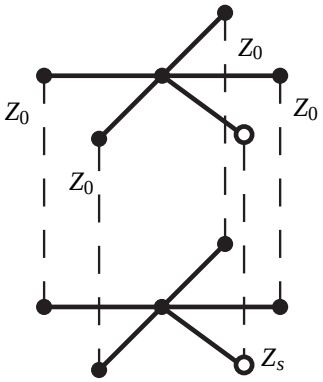

Figure 2.2: The 2D TLM cell center with a shunt stub line connection with reference impedance Z_s.

and

$$\gamma = \frac{2}{4 + \frac{Y_s}{Y_0}}, \tag{2.25c}$$

$$\gamma_s = \frac{2\frac{Y_s}{Y_0}}{4 + \frac{Y_s}{Y_0}}. \tag{2.25d}$$

Inserting (2.25c) and (2.25d) into (2.25a) we obtain the expression for the scattering matrix

$$\mathbf{S} = \frac{1}{\hat{Y}} \begin{bmatrix} (2-\hat{Y}) & 2 & 2 & 2 & 2\frac{Y_s}{Y_0} \\ 2 & (2-\hat{Y}) & 2 & 2 & 2\frac{Y_s}{Y_0} \\ 2 & 2 & (2-\hat{Y}) & 2 & 2\frac{Y_s}{Y_0} \\ 2 & 2 & 2 & (2-\hat{Y}) & 2\frac{Y_s}{Y_0} \\ 2 & 2 & 2 & 2 & (2\frac{Y_s}{Y_0} - \hat{Y}) \end{bmatrix}, \tag{2.25e}$$

where

$$\hat{Y} = 4 + \frac{Y_s}{Y_0}. \tag{2.25f}$$

The expression (2.25e) is the well-known scattering matrix of the 2D TLM shunt node with a shunt stub line (cf., e.g., [26], p. 97).

2.3.1 Two-dimensional TLM cell

For the relation between electrical network quantities and electromagnetic field quantities discrete exterior calculus is applied. Discrete exterior calculus also introduces the discrete exterior derivative, the discrete counterpart of the exterior derivative operator.

The network quantities are obtained from the electromagnetic quantities taking the integrals of them. This is equivalent to what is also called finite integrals. However, in contrast to finite integrals, the underlying structure of the manifolds is maintained.

Let us take a look at 2D example. We assume invariance of the electromagnetic field with respect to z direction, i.e., $\frac{\partial}{\partial z} = 0$. Consequently, only

2D problem description is appropriate. Furthermore, the TM_z modes are considered for now.

Using differential forms notations, the electromagnetic phenomena of TM_z modes in free-space (ε_0, μ_0) is described with the following reduced Maxwell's equations

$$\left(\frac{\partial H_y}{\partial x} - \frac{\partial H_x}{\partial y}\right) \mathrm{d}x \wedge \mathrm{d}y = \varepsilon_0 \frac{\partial E_z}{\partial t} \mathrm{d}x \wedge \mathrm{d}y, \tag{2.26a}$$

$$\frac{\partial E_z}{\partial x} \mathrm{d}z \wedge \mathrm{d}x = \mu_0 \frac{\partial H_y}{\partial t} \mathrm{d}z \wedge \mathrm{d}x, \tag{2.26b}$$

$$\frac{\partial E_z}{\partial y} \mathrm{d}y \wedge \mathrm{d}z = -\mu_0 \frac{\partial H_x}{\partial t} \mathrm{d}y \wedge \mathrm{d}z. \tag{2.26c}$$

The unit one-forms $\mathrm{d}x$, $\mathrm{d}y$, $\mathrm{d}z$, their wedge product and the Hodge operator can be visualized as shown in Figure 2.3.

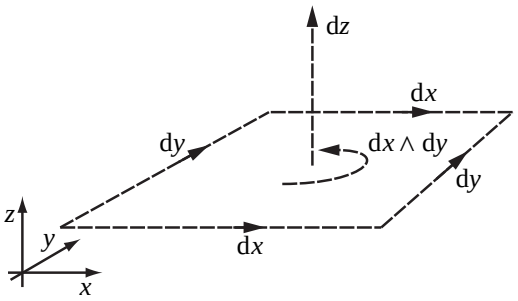

Figure 2.3: Unit one-forms $\mathrm{d}x$, $\mathrm{d}y$, $\mathrm{d}z$ and the two-form $\mathrm{d}x \wedge \mathrm{d}y = \star\,\mathrm{d}z$ in an Euclidean three-dimensional space.

The discrete counterparts of the unit one-forms are the discrete one-forms Δx, Δy and Δz. Similarly to the differential forms, we may define for the discrete forms the wedge product, the Hodge operator and the discrete exterior derivative operation [27].

We introduce a mapping from electromagnetic field quantities to network quantities. The mapping is shown in Figure 2.5. We assign to each

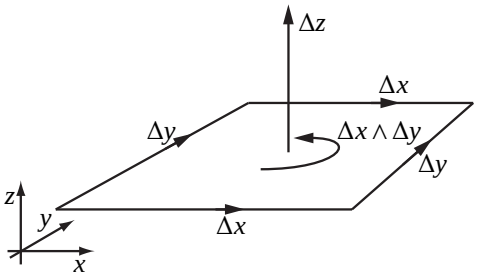

Figure 2.4: Discrete one-forms Δx, Δy, Δz and the two-form $\Delta x \wedge \Delta y = \star \Delta z$ in an Euclidean three-dimensional space.

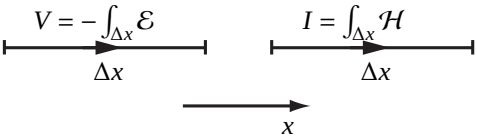

Figure 2.5: Mapping from electromagnetic field quantities to network quantities.

oriented line of the TLM cell two network quantities: *voltage* and *current*. The resulting 2D TLM cell with assigned network quantities is show in Figure 2.6.

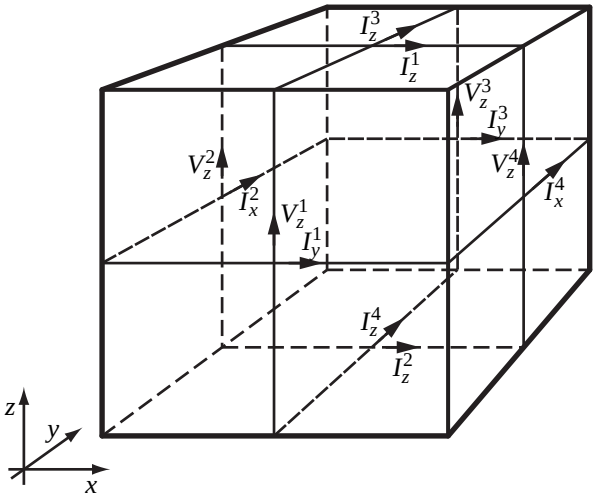

Figure 2.6: 2D TLM cell with assigned network quantities for TM modes.

The expressions for discrete exterior derivatives of TM field with the introduced network quantities can be written as

$$\mathrm{d}\mathcal{H}|_{xy} = I_y^1 + I_x^4 - I_y^3 - I_x^2, \tag{2.27a}$$

$$\mathrm{d}\mathcal{H}|_{zx} = I_z^1 - I_z^2 = 0, \qquad \text{since } \frac{\partial I_z}{\partial z} = 0, \tag{2.27b}$$

$$\mathrm{d}\mathcal{H}|_{yz} = I_z^4 - I_z^3 = 0, \qquad \text{since } \frac{\partial I_z}{\partial z} = 0, \tag{2.27c}$$

$$\mathrm{d}\mathcal{E}|_{xy} = 0, \tag{2.27d}$$

$$\mathrm{d}\mathcal{E}|_{zx} = V_z^2 - V_z^4, \tag{2.27e}$$

$$\mathrm{d}\mathcal{E}|_{yz} = V_z^3 - V_z^1. \tag{2.27f}$$

The invariance of macroscopic quantities (field intensities, voltages and currents) to the scattering process – with the assumption of the scattering process taking place inside the TLM cell center – and the frequency-independence of the scattering matrix imply that $\frac{\partial}{\partial t} = 0$ in the Maxwell's equations (2.26). With this assumption the equations which must be satisfied during the scattering process are

$$\left(\frac{\partial H_y}{\partial x} - \frac{\partial H_x}{\partial y}\right) \mathrm{d}x \wedge \mathrm{d}y = \mathrm{d}\mathcal{H}|_{xy} = 0, \tag{2.28a}$$

$$\frac{\partial E_z}{\partial x} \mathrm{d}z \wedge \mathrm{d}x = \mathrm{d}\mathcal{E}|_{zx} = 0, \tag{2.28b}$$

$$\frac{\partial E_z}{\partial y} \mathrm{d}y \wedge \mathrm{d}z = \mathrm{d}\mathcal{E}|_{yz} = 0. \tag{2.28c}$$

These are the equations of static electric and magnetic fields.

Inserting the expressions for discrete exterior derivatives in terms of network quantities (2.27) into (2.28) we get

$$I_y^1 + I_x^4 - I_y^3 - I_x^2 = 0, \tag{2.29a}$$

$$V_z^2 - V_z^4 = 0 \quad \Rightarrow \quad V_z^2 = V_z^4, \tag{2.29b}$$

$$V_z^3 - V_z^1 = 0 \quad \Rightarrow \quad V_z^3 = V_z^1, \tag{2.29c}$$

Equation (2.29a) can be identified as Kirchhoff's current law (KCL) (see also Figure 2.7). The resulting 2D TLM cell center with assigned network quantities is show in Figure 2.8.

Since the equations (2.28) describe static fields, any integral on a closed path must equal to zero. Taking the integral on a closed path as shown in Figure 2.9 results in the following additional condition

$$V_z^1 - V_z^4 + V_z^3 - V_z^2 = 0 \quad \Rightarrow \quad V_z^1 + V_z^3 = V_z^4 + V_z^2. \tag{2.30}$$

From (2.29) we know that $V_z^1 = V_z^3$ and $V_z^4 = V_z^2$ so we obtain the condition

$$V_z^1 = V_z^2 = V_z^3 = V_z^4. \tag{2.31}$$

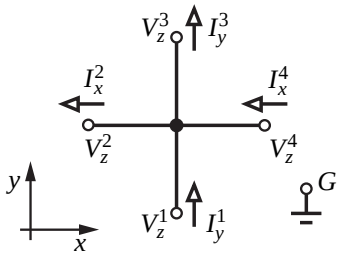

Figure 2.7: KCL and KVL for the 2D TLM cell center.

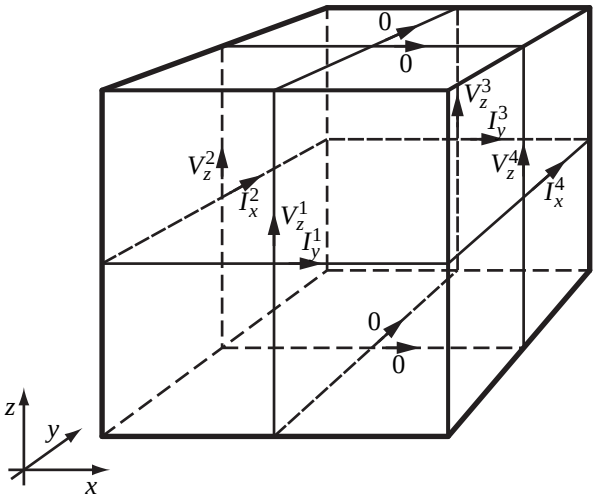

Figure 2.8: 2D TLM cell center with assigned network quantities for TM modes.

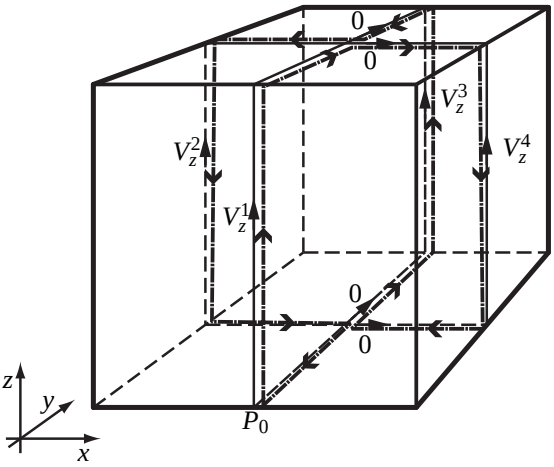

Figure 2.9: Integration path.

The network quantities may be transformed to wave quantities using the following transformation rules

$$V_z^1 = a_1 + b_1, \tag{2.32a}$$
$$V_z^2 = a_2 + b_2, \tag{2.32b}$$
$$V_z^3 = a_3 + b_3, \tag{2.32c}$$
$$V_z^4 = a_4 + b_4, \tag{2.32d}$$
$$I_y^1 = a_1 - b_1, \tag{2.32e}$$
$$I_x^2 = -a_2 + b_2, \tag{2.32f}$$
$$I_y^3 = -a_3 + b_3, \tag{2.32g}$$
$$I_x^4 = a_4 - b_4. \tag{2.32h}$$

Inserting (2.32) into (2.29) and (2.31) we obtain the following set of

linearly independent equations

$$a_1 + a_4 + a_3 + a_2 = b_1 + b_4 + b_3 + b_2, \tag{2.33a}$$
$$a_3 + b_3 = a_1 + b_1, \tag{2.33b}$$
$$a_2 + b_2 = a_4 + b_4, \tag{2.33c}$$
$$a_1 + b_1 = a_2 + b_2. \tag{2.33d}$$

Instead of (2.33d) we can also take the equation

$$a_3 + b_3 = a_4 + b_4 \tag{2.33e}$$

without a change in the result. Defining the vectors of incoming and outgoing waves

$$\mathbf{a} = (a_1, a_2, a_3, a_4)^T, \tag{2.34a}$$
$$\mathbf{b} = (b_1, b_2, b_3, b_4)^T, \tag{2.34b}$$

we can write (2.33) as

$$\mathbf{Aa} = \mathbf{Bb}, \tag{2.35}$$

with

$$\mathbf{A} = \begin{bmatrix} 1 & 1 & 1 & 1 \\ -1 & 0 & 1 & 0 \\ 0 & 1 & 0 & -1 \\ 1 & -1 & 0 & 0 \end{bmatrix}, \tag{2.36a}$$

$$\mathbf{B} = \begin{bmatrix} 1 & 1 & 1 & 1 \\ 1 & 0 & -1 & 0 \\ 0 & -1 & 0 & 1 \\ -1 & 1 & 0 & 0 \end{bmatrix}. \tag{2.36b}$$

Using the definition of scattering matrix, i.e., $\mathbf{b} = \mathbf{Sa}$, and with (2.35), we see that the scattering matrix can be computed from matrices $\mathbf{A}$ and $\mathbf{B}$ as follows

$$\mathbf{S} = \mathbf{B}^{-1}\mathbf{A}. \tag{2.37}$$

With the inverse of $\mathbf{B}$ given by

$$\mathbf{B}^{-1} = \frac{1}{4}\begin{bmatrix} 1 & 1 & -1 & -2 \\ 1 & 1 & -1 & 2 \\ 1 & -3 & -1 & -2 \\ 1 & 1 & 3 & 2 \end{bmatrix} \tag{2.38}$$

we obtain the scattering matrix

$$\begin{aligned} \mathbf{S} &= \frac{1}{4}\begin{bmatrix} 1 & 1 & -1 & -2 \\ 1 & 1 & -1 & 2 \\ 1 & -3 & -1 & -2 \\ 1 & 1 & 3 & 2 \end{bmatrix} \cdot \begin{bmatrix} 1 & 1 & 1 & 1 \\ -1 & 0 & 1 & 0 \\ 0 & 1 & 0 & -1 \\ 1 & -1 & 0 & 0 \end{bmatrix} \\ &= \frac{1}{2}\begin{bmatrix} -1 & 1 & 1 & 1 \\ 1 & -1 & 1 & 1 \\ 1 & 1 & -1 & 1 \\ 1 & 1 & 1 & -1 \end{bmatrix}, \end{aligned} \tag{2.39}$$

which is the well-known scattering matrix of the 2D shunt TLM node (cf., e.g., [26], p. 95).

Dual to the TM modes are TE modes. The derivation of the scattering matrix for 2D TE modes follows the same steps as for the TM modes and will be presented briefly. The 2D TLM cell center for TE modes is shown in Figure 2.10.

The independent set of linear equations obtained from the equations $\mathrm{d}\mathcal{E} = 0$ and $\mathrm{d}\mathcal{H} = 0$ using the discrete exterior calculus on regular rectangular mesh is given by

$$V_x^1 + V_y^4 - V_x^3 - V_y^2 = 0, \tag{2.40a}$$

$$I_y^3 - I_y^1 = 0, \tag{2.40b}$$

$$I_x^2 - I_x^4 = 0, \tag{2.40c}$$

$$I_y^1 - I_x^4 + I_y^3 - I_x^2 = 0. \tag{2.40d}$$

Equation (2.40a) is derived from $\mathrm{d}\mathcal{E} = 0$ and equations (2.40b) and (2.40c) are derived from $\mathrm{d}\mathcal{H} = 0$. The derivation of (2.40d) follows the same procedure of deriving (2.30).

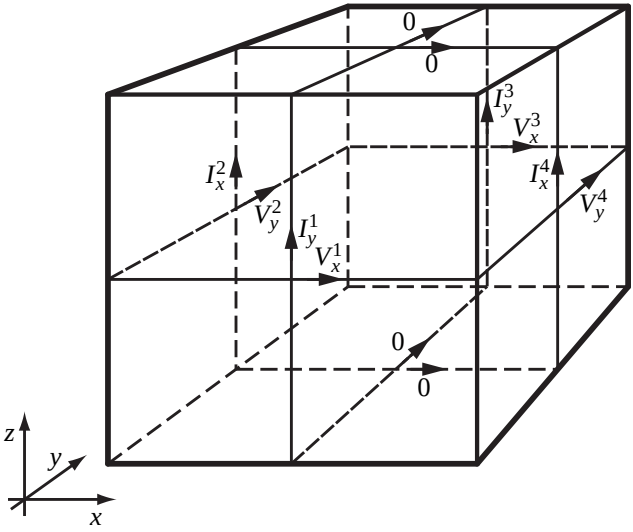

Figure 2.10: 2D TLM cell center with assigned network quantities for TE modes.

The transformation from network quantities to wave quantities is defined by

$$V_x^1 = a_1 + b_1, \tag{2.41a}$$
$$V_y^2 = a_2 + b_2, \tag{2.41b}$$
$$V_x^3 = a_3 + b_3, \tag{2.41c}$$
$$V_y^4 = a_4 + b_4, \tag{2.41d}$$
$$I_y^1 = -a_1 + b_1, \tag{2.41e}$$
$$I_x^2 = a_2 - b_2, \tag{2.41f}$$
$$I_y^3 = a_3 - b_3, \tag{2.41g}$$
$$I_x^4 = -a_4 + b_4. \tag{2.41h}$$

With the definitions (2.34) and (2.41), equations (2.40) are written in the form of (2.35), where

$$\mathbf{A} = \begin{bmatrix} 1 & -1 & -1 & 1 \\ 1 & 0 & 1 & 0 \\ 0 & 1 & 0 & 1 \\ -1 & -1 & 1 & 1 \end{bmatrix}, \tag{2.42a}$$

$$\mathbf{B} = \begin{bmatrix} -1 & 1 & 1 & -1 \\ 1 & 0 & 1 & 0 \\ 0 & 1 & 0 & 1 \\ -1 & -1 & 1 & 1 \end{bmatrix} \tag{2.42b}$$

and the inverse matrix of the matrix $\mathbf{B}$ is

$$\mathbf{B}^{-1} = \frac{1}{4} \begin{bmatrix} -1 & 2 & 0 & -1 \\ 1 & 0 & 2 & -1 \\ 1 & 2 & 0 & 1 \\ -1 & 0 & 2 & 1 \end{bmatrix}. \tag{2.42c}$$

The scattering matrix obtained from $\mathbf{S} = \mathbf{B}^{-1}\mathbf{A}$ reads

$$\mathbf{S} = \frac{1}{2}\begin{bmatrix} 1 & 1 & 1 & -1 \\ 1 & 1 & -1 & 1 \\ 1 & -1 & 1 & 1 \\ -1 & 1 & 1 & 1 \end{bmatrix}, \tag{2.43}$$

which is the scattering matrix of the 2D series TLM node (cf., e.g., [26], p. 78).

2.3.2 Three-dimensional TLM cell

The scattering matrix of the 3D symmetrical condensed TLM node is obtained using the same techniques as in the previous section. However, in the 3D case no decomposition into TE and TM field is possible. Consequently, the field intensities are considered with all components, i.e.,

$$\mathcal{E} = E_x\,\mathrm{d}x + E_y\,\mathrm{d}y + E_z\,\mathrm{d}z, \tag{2.44a}$$
$$\mathcal{H} = H_x\,\mathrm{d}x + H_y\,\mathrm{d}y + H_z\,\mathrm{d}z. \tag{2.44b}$$

The network quantities are obtained from the electromagnetic field quantities in the same way as described in the two-dimensional case. The 3D TLM cell is shown in Figure 2.11.

The following are the 12 linearly independent equations which must be

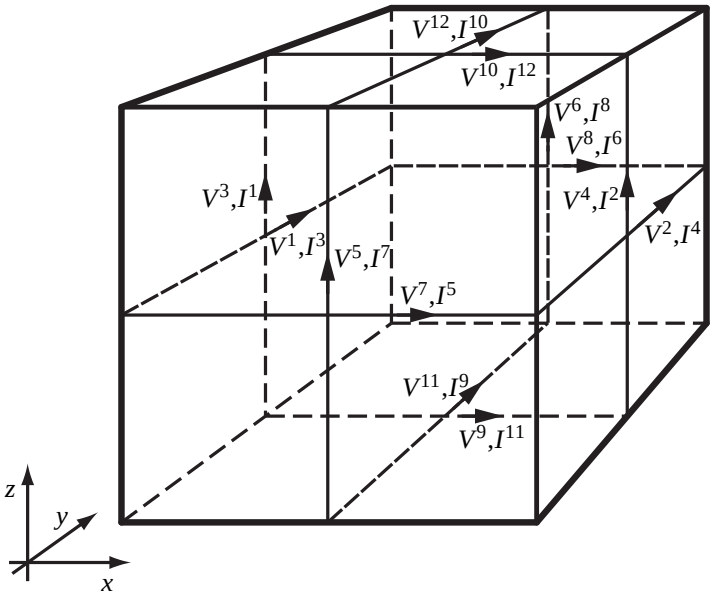

Figure 2.11: 3D TLM cell with assigned network quantities.

satisfied by the network quantities inside the symmetrical condensed node.

$$V^7 + V^2 - V^8 - V^1 = 0, \tag{2.45a}$$
$$I^5 + I^4 - I^6 - I^3 = 0, \tag{2.45b}$$
$$V^{11} + V^6 - V^{12} - V^5 = 0, \tag{2.45c}$$
$$I^9 + I^8 - I^{10} - I^7 = 0, \tag{2.45d}$$
$$V^3 + V^{10} - V^4 - V^9 = 0, \tag{2.45e}$$
$$I^1 + I^{12} - I^2 - I^{11} = 0, \tag{2.45f}$$
$$V^5 + V^6 - V^4 - V^3 = 0, \tag{2.45g}$$
$$V^7 + V^8 - V^{10} - V^9 = 0, \tag{2.45h}$$
$$V^1 + V^2 - V^{12} - V^{11} = 0, \tag{2.45i}$$
$$I^7 + I^8 - I^1 - I^2 = 0, \tag{2.45j}$$
$$I^5 + I^6 - I^{12} - I^{11} = 0, \tag{2.45k}$$
$$I^3 + I^4 - I^{10} - I^9 = 0. \tag{2.45l}$$

The transformations from wave quantities to network quantities are defined by the following equations.

$$V^i = a_i + b_i, \tag{2.46a}$$

where $i = 1 \ldots 12$ and

$$I^1 = a_1 - b_1, \tag{2.46b}$$
$$I^2 = -a_2 + b_2, \tag{2.46c}$$
$$I^3 = -a_3 + b_3, \tag{2.46d}$$
$$I^4 = a_4 - b_4, \tag{2.46e}$$
$$I^5 = a_5 - b_5, \tag{2.46f}$$
$$I^6 = -a_6 + b_6, \tag{2.46g}$$
$$I^7 = -a_7 + b_7, \tag{2.46h}$$
$$I^8 = a_8 - b_8, \tag{2.46i}$$
$$I^9 = a_9 - b_9, \tag{2.46j}$$
$$I^{10} = -a_{10} + b_{10}, \tag{2.46k}$$
$$I^{11} = -a_{11} + b_{11}, \tag{2.46l}$$
$$I^{12} = a_{12} - b_{12}. \tag{2.46m}$$

The matrices **A** and **B** for the three-dimensional case read

$$\mathbf{A} = \begin{bmatrix} -1 & 1 & 0 & 0 & 0 & 0 & 1 & -1 & 0 & 0 & 0 & 0 \\ 0 & 0 & 1 & 1 & 1 & 1 & 0 & 0 & 0 & 0 & 0 & 0 \\ 0 & 0 & 0 & 0 & -1 & 1 & 0 & 0 & 0 & 0 & 1 & -1 \\ 0 & 0 & 0 & 0 & 0 & 0 & 1 & 1 & 1 & 1 & 0 & 0 \\ 0 & 0 & 1 & -1 & 0 & 0 & 0 & 0 & -1 & 1 & 0 & 0 \\ 1 & 1 & 0 & 0 & 0 & 0 & 0 & 0 & 0 & 0 & 1 & 1 \\ 0 & 0 & -1 & -1 & 1 & 1 & 0 & 0 & 0 & 0 & 0 & 0 \\ 0 & 0 & 0 & 0 & 0 & 1 & 1 & -1 & -1 & 0 & 0 & 0 \\ 1 & 1 & 0 & 0 & 0 & 0 & 0 & 0 & 0 & 0 & -1 & -1 \\ -1 & 1 & 0 & 0 & 0 & 0 & -1 & 1 & 0 & 0 & 0 & 0 \\ 0 & 0 & 0 & 0 & 1 & -1 & 0 & 0 & 0 & 0 & 1 & -1 \\ 0 & 0 & -1 & 1 & 0 & 0 & 0 & 0 & -1 & 1 & 0 & 0 \end{bmatrix}, \tag{2.47a}$$

$$\mathbf{B} = \begin{bmatrix} 1 & -1 & 0 & 0 & 0 & 0 & -1 & 1 & 0 & 0 & 0 & 0 \\ 0 & 0 & 1 & 1 & 1 & 1 & 0 & 0 & 0 & 0 & 0 & 0 \\ 0 & 0 & 0 & 0 & 1 & -1 & 0 & 0 & 0 & 0 & -1 & 1 \\ 0 & 0 & 0 & 0 & 0 & 0 & 1 & 1 & 1 & 1 & 0 & 0 \\ 0 & 0 & -1 & 1 & 0 & 0 & 0 & 0 & 1 & -1 & 0 & 0 \\ 1 & 1 & 0 & 0 & 0 & 0 & 0 & 0 & 0 & 0 & 1 & 1 \\ 0 & 0 & 1 & 1 & -1 & -1 & 0 & 0 & 0 & 0 & 0 & 0 \\ 0 & 0 & 0 & 0 & 0 & -1 & -1 & 1 & 1 & 0 & 0 & 0 \\ -1 & -1 & 0 & 0 & 0 & 0 & 0 & 0 & 0 & 0 & 1 & 1 \\ -1 & 1 & 0 & 0 & 0 & 0 & -1 & 1 & 0 & 0 & 0 & 0 \\ 0 & 0 & 0 & 0 & 1 & -1 & 0 & 0 & 0 & 0 & 1 & -1 \\ 0 & 0 & -1 & 1 & 0 & 0 & 0 & 0 & -1 & 1 & 0 & 0 \end{bmatrix} \tag{2.47b}$$

The scattering matrix of the 3D TLM node for free-space is computed from $\mathbf{S} = \mathbf{B}^{-1}\mathbf{A}$ and reads

$$\mathbf{S} = \frac{1}{2}\begin{bmatrix} 0 & 0 & 0 & 0 & 0 & 0 & 1 & -1 & 0 & 0 & 1 & 1 \\ 0 & 0 & 0 & 0 & 0 & 0 & -1 & 1 & 0 & 0 & 1 & 1 \\ 0 & 0 & 0 & 0 & 1 & 1 & 0 & 0 & 1 & -1 & 0 & 0 \\ 0 & 0 & 0 & 0 & 1 & 1 & 0 & 0 & -1 & 1 & 0 & 0 \\ 0 & 0 & 1 & 1 & 0 & 0 & 0 & 0 & 0 & 0 & 1 & -1 \\ 0 & 0 & 1 & 1 & 0 & 0 & 0 & 0 & 0 & 0 & -1 & 1 \\ 1 & -1 & 0 & 0 & 0 & 0 & 0 & 0 & 1 & 1 & 0 & 0 \\ -1 & 1 & 0 & 0 & 0 & 0 & 0 & 0 & 1 & 1 & 0 & 0 \\ 0 & 0 & 1 & -1 & 0 & 0 & 1 & 1 & 0 & 0 & 0 & 0 \\ 0 & 0 & -1 & 1 & 0 & 0 & 1 & 1 & 0 & 0 & 0 & 0 \\ 1 & 1 & 0 & 0 & 1 & -1 & 0 & 0 & 0 & 0 & 0 & 0 \\ 1 & 1 & 0 & 0 & -1 & 1 & 0 & 0 & 0 & 0 & 0 & 0 \end{bmatrix} \tag{2.48}$$

2.4 Discrete Source Modeling

For the modeling of antenna problems discrete sources are of importance. Since the TLMME method is applied to radiating problems, a suitable

modeling of discrete sources is needed. In this section the source port based on wave digital filters and *boundary oriented field mapping* [16] is described and it will be shown how it can be applied to model a discrete source distributed over more TLM cells.

As was shown in Section 2.3, the 2D TLM method and in particular the scattering matrix are related to the parallel and series adaptors of wave digital filters. Here we use this relation to describe a discrete port for the TLM method.

The connection network based on parallel and series adaptors of WDFs can be used for the modeling of discrete sources. The connection network is an $N+1$ port network with *N TLM ports* connected to the TLM mesh and one *source port*. The source port is the input port to the TLM model.

The TLM ports of the connection network are connected to the TLM link lines at the interfaces between adjacent TLM cells. Consequently, the mapping type between network and field quantities is the boundary oriented field mapping. Schematic pictures of canonic parallel and series connection networks exciting one field polarization are shown in Figure 2.12 and Figure 2.13.

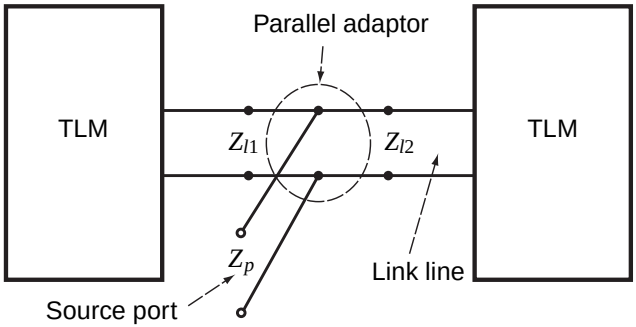

Figure 2.12: Canonic parallel connection subnetwork; the reference impedances of the TLM link lines are Z_{l1} and Z_{l2} and the reference impedance of the source port is Z_p.

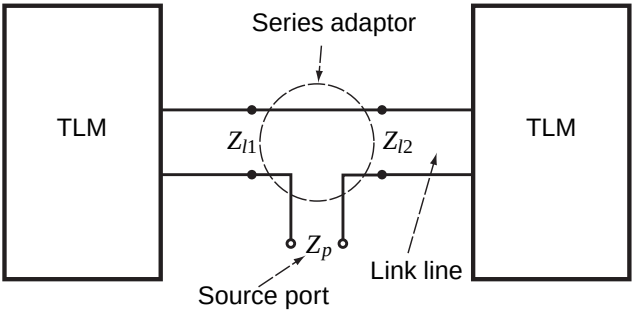

Figure 2.13: Canonic series connection subnetwork; the reference impedances of the TLM link lines are Z_{l1} and Z_{l2} and the reference impedance of the source port is Z_p.

We can see that the discrete voltage port for one polarization can be seen as parallel adaptor placed at the interface of two TLM link lines.

The parallel connection network has the following properties:

1. A common voltage (i.e., electric field intensity) is impressed at the interface between adjacent TLM cells.

2. Different line impedances of the TLM link lines and the source port are taken into account.

3. The scattering matrix of the connection network is

   - real,
   - frequency independent,
   - energy conservative,
   - time-reversible and
   - the eigenvalues equal ±1. If all the TLM port impedances and the source port impedance are equal then the scattering matrix is also unitary and symmetric.

A series connection network is dual to the parallel connection network. The properties of the series connection network are the same as those of the parallel one except that a common current (i.e., magnetic field intensity) is impressed at the interface between adjacent TLM cells.

A series port is dual to the parallel port and is shown in Figure 2.13. The properties of the series discrete port are

1. A common current (i.e., magnetic field intensity) is impressed at the interface.

2. Different line impedances of the link lines and the discrete port are taken into account by the adaptor.

3. The series adaptor is characterized by a (3×3) scattering matrix with the same properties as for the parallel adaptor

To the discrete port three different source types can be connected. These are

1. ideal voltage source,

2. ideal current source,

3. power source with defined internal impedance.

The different source types are shown in Figure 2.14.

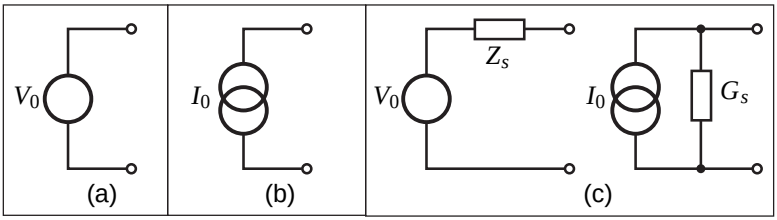

Figure 2.14: Lumped sources which may be connected to the discrete port adaptor.

The WDF realizations of these sources can be connected directly to the source port of the connection network. The WDF realizations of the different source types with wave digital filters are shown in Figure 2.15. We use here the same convention for symbols of WDF adaptors and wave flow diagrams as in [25].

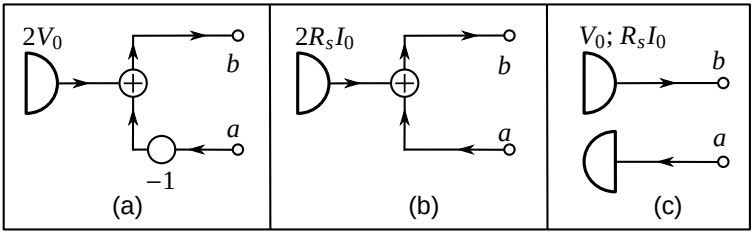

Figure 2.15: WDF representations of the sources.

The power source can also be seen (using Thévenin theorem) as an ideal voltage source connected at infinity to one end of a transmission line with impedance Z_S. The other end of the transmission line is connected to the discrete port.

The discrete port just described implements following features into the TLM algorithm:

- Well-defined excitation of field amplitudes and energy.
- Impulsive characterization of electromagnetic structures with linear properties. This is possible since only one port is available from "outside" and the TLM model is linear.
- Direct calculation of scattering parameters from the incoming and reflected wave amplitudes.

An example on impulsive excitation of bowtie antenna is given in Section 6.3.

2.4.1 Example – canonic parallel connection network

The scattering matrix referred to the port impedance $Z_p = \frac{377}{2}\ \Omega$ with $Z_{l1} = Z_{l2} = 377\,\Omega$ reads

$$\mathbf{S}_p = \begin{bmatrix} 0 & \frac{1}{2} & \frac{1}{2} \\ 1 & -\frac{1}{2} & \frac{1}{2} \\ 1 & \frac{1}{2} & -\frac{1}{2} \end{bmatrix}. \tag{2.49}$$

The scattering matrix referred to the port impedance $Z_p = 50\ \Omega$ with $Z_{l1} = Z_{l2} = 377\ \Omega$ reads

$$\mathbf{S}_p = \begin{bmatrix} 0.58071 & 0.20964 & 0.20964 \\ 1.58071 & -0.79036 & 0.20964 \\ 1.58071 & 0.20964 & -0.79036 \end{bmatrix}. \tag{2.50}$$

It is easy to check that $\mathbf{S}_p\mathbf{S}_p = \mathbf{I}$ and $|\det(\mathbf{S}_p)| = 1$. The matrices are thus valid scattering matrix of the TLM method.

3 Multipole Expansion

In the multipole expansion the total radiated electromagnetic field is expressed as linear combinations of known basis one-forms, called *radiation modes*. In homogeneous medium the radiation modes form a complete orthonormal set of basis one-forms. These are considered to have an infinitesimally small source in the center of the coordinate system used for the expansion which makes them behave singularly there. Hence the name multipole expansion.

For the expansion we use the spherical coordinate system (r, ϑ, φ) – (radius, elevation, azimuth) – see also Figure 3.1. We decompose the total field into transverse and longitudinal parts $\underline{\mathcal{N}} = \underline{\mathcal{N}}_t + \underline{N}_r \,\mathrm{d}r$ with $\underline{\mathcal{N}}_t = \underline{N}_\vartheta r \,\mathrm{d}\vartheta + \underline{N}_\varphi r \sin\vartheta \,\mathrm{d}\varphi$, where $\underline{\mathcal{N}}$ stands for the one-form field intensity phasors $\underline{\mathcal{E}}$ or $\underline{\mathcal{H}}$. Phasor quantities are distinguished by underlined font.

It is shown in [28], that it is sufficient to expand only the transverse parts of the total field. These are the independent field quantities from which the radial (longitudinal) components can be computed.

Based on these considerations we write the tangential field intensities as

$$\mathcal{E}_t(r,\vartheta,\varphi,t) = \sum_p V_p(r,t)\, e_p(\vartheta,\varphi), \tag{3.1a}$$

$$\mathcal{H}_t(r,\vartheta,\varphi,t) = \sum_p I_p(r,t) h_p(\vartheta,\varphi) = \sum_p I_p(r,t)\,(\perp_n e_p(\vartheta,\varphi)), \tag{3.1b}$$

where $V_p(r,t)$ and $I_p(r,t)$ are *generalized voltages* and *generalized currents*, respectively, and $e_p(\vartheta,\varphi)$ and $h_p(\vartheta,\varphi)$ are the transverse basis one-forms of the electric field intensity and the magnetic field intensity, respectively, corresponding to the mode p. The mode index p summarizes four indices (n,m,i,s), the meaning of which will be given later in Section 3.1.

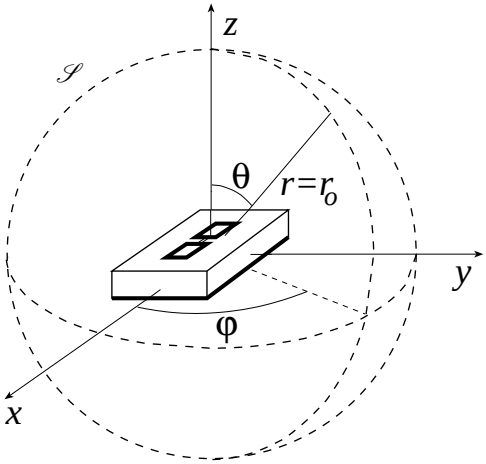

Figure 3.1: Electromagnetic structure embedded into a virtual spherical manifold $\mathscr{S}$ of radius $r = r_0$.

In (3.1) we use the twist operator $\perp_n$, defined in [11] for a general one-form $\mathcal{A}$ as

$$\perp_n \mathcal{A} = \star(n \wedge \mathcal{A}), \tag{3.2a}$$

where $\star$ is the Hodge operator and $\wedge$ denotes the wedge product.

A local picture of the twist operator acting on a general one-form $\mathcal{A}$ is shown in Figure 3.2. The two-form $n \wedge \mathcal{A}$ is shown as an oriented surface. We can see also the tangential part of the one-form $\mathcal{A}$ with respect to the normal direction n defined as

$$(\mathcal{A})_t = n \lrcorner (n \wedge A), \tag{3.2b}$$

where the angle operator $\lrcorner$ denotes the contraction (for more details see [29]).

The normal one-form n is normal to the direction of a spherical manifold $\mathscr{S}(r)$ with a given radius r and forms a rectangular frame with the two normal one-forms u and v, which are tangential to the surface of the

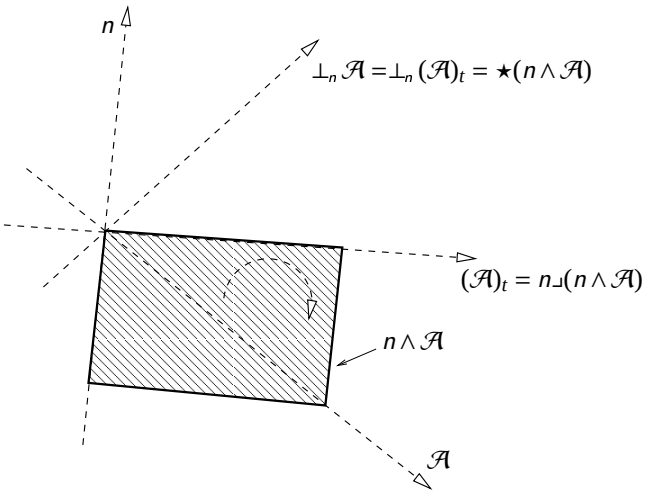

Figure 3.2: A local picture of the twisted one-form $\perp_n \mathcal{A}$.

manifold. This is shown in Figure 3.3. The unit normal one-form n may be written as

$$n = n_x \, \mathrm{d}x + n_y \, \mathrm{d}y + n_z \, \mathrm{d}z = \mathrm{d}r, \tag{3.3a}$$

with

$$\begin{aligned} n_x^2 + n_y^2 + n_z^2 &= \left(\frac{\partial r}{\partial x}\right)^2 + \left(\frac{\partial r}{\partial y}\right)^2 + \left(\frac{\partial r}{\partial z}\right)^2 = \\ &= \left(\pm \frac{x}{\sqrt{x^2+y^2+z^2}}\right)^2 + \left(\pm \frac{y}{\sqrt{x^2+y^2+z^2}}\right)^2 + \left(\pm \frac{z}{\sqrt{x^2+y^2+z^2}}\right)^2 = \\ &= 1. \end{aligned} \tag{3.3b}$$

We can see from (3.1) that the transverse basis one-forms of the magnetic field intensity can be obtained from the transverse basis one-forms of the electric field intensity. The generalized voltages and currents for each

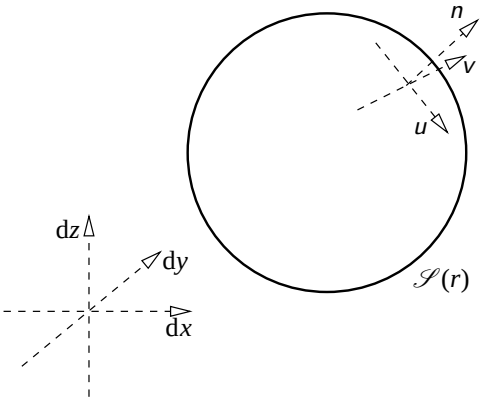

Figure 3.3: Spherical manifold $\mathscr{S}(r)$ with the tangent frame n, u and v.

mode p may be obtained from the total field intensities by integration over the spherical manifold $\mathscr{S}(r)$ with radius r by

$$V_p(r,t) = \iint_{\mathscr{S}(r)} (-\perp_n \mathcal{E}(r,\vartheta,\varphi,t)) \wedge e_p(\vartheta,\varphi), \tag{3.4a}$$

$$I_p(r,t) = \iint_{\mathscr{S}(r)} -\mathcal{H}(r,\vartheta,\varphi,t) \wedge e_p(\vartheta,\varphi). \tag{3.4b}$$

The generalized voltages are related to the generalized currents by *generalized impedances*. In time-domain the relation is given by

$$V_p(r,t) = Z_p(r,t) * I_p(r,t), \tag{3.5}$$

where $*$ denotes the convolution in time. The generalized impedance $Z_p(r,t)$ describes completely the coupling between the electric and magnetic field intensities. The generalized impedance is r dependent due to the varying cross section of the half-space given by $r \geq r_0$ for a given radius $r = r_0$

Assuming harmonic excitation, the frequency domain representations of the field quantities and the generalized network quantities can be used.

Using the phasor representations for the field quantities the relation (3.5) reads

$$\underline{V}_p(r,\omega) = \underline{Z}_p(r,\omega)\underline{I}_p(r,\omega). \tag{3.6}$$

3.1 Radiation Modes

The transverse magnetic (TM) and transverse electric (TE) radiation modes are derived from the magnetic one-form potential $\underline{\mathcal{A}}$ and the electric one-form potential $\underline{\mathcal{F}}$, respectively, which are oriented in the dr direction

$$\underline{\mathcal{A}} = \underline{A}_r\,\mathrm{d}r = r\psi\,\mathrm{d}r, \quad \underline{\mathcal{F}} = \underline{F}_r\,\mathrm{d}r = r\psi\,\mathrm{d}r. \tag{3.7}$$

In (3.7), ψ is a scalar function of spherical coordinates satisfying the scalar Helmholtz equation

$$(\star\mathrm{d}\star\mathrm{d} + k^2)\psi(r,\vartheta,\varphi) = 0 \tag{3.8}$$

in spherical coordinate system, where $k = \omega\sqrt{\varepsilon\mu}$ is the wavenumber, ω the angular frequency and ε and μ the permittivity and permeability of the background space, respectively.

The field intensities of the TM radiation modes are obtained from the magnetic vector potential $\underline{\mathcal{A}}$ by

$$\underline{\mathcal{H}} = \star\mathrm{d}\underline{\mathcal{A}}, \qquad \underline{\mathcal{E}} = \frac{1}{j\omega\varepsilon}\star\mathrm{d}\star\mathrm{d}\underline{\mathcal{A}}. \tag{3.9a}$$

The field intensities of the TE radiation modes are obtained from the electric vector potential $\underline{\mathcal{F}}$ by

$$\underline{\mathcal{E}} = -\star\mathrm{d}\underline{\mathcal{F}}, \qquad \underline{\mathcal{H}} = \frac{1}{j\omega\mu}\star\mathrm{d}\star\mathrm{d}\underline{\mathcal{F}}. \tag{3.9b}$$

The general solution of (3.8), obtained by separation of variables technique, is given by

$$\psi(r,\vartheta,\varphi) = b_n(kr)L_n^m(\cos\vartheta)h(m\varphi), \tag{3.10}$$

where $b_n(kr)$ are the spherical Bessel functions, $L_n^m(\cos\vartheta)$ the associated Legendre functions and $h(m\varphi)$ the harmonic functions. Due to the properties of the functions $h(m\varphi)$ and $L_n^m(\cos\vartheta)$, and if we restrict our considerations to physically allowed solutions, we have to choose n and m integer, with $n = 0, 1, 2, \ldots$ and $0 \le m \le n$.

We assume that all sources are confined within the spherical simulation region. Therefore, outside the sphere only outward propagating waves occur and the Sommerfeld radiation condition is fulfilled. Thus, we take $b_n(kr) = h_n^{(2)}(kr)$ in (3.10), with $h_n^{(2)}(kr)$ being the spherical Hankel functions of the second kind.

We define *real spherical harmonics* $Y_{nm}^i(\vartheta,\varphi)$ with $n = 0, 1, 2, \ldots$, $0 \le m \le n$ and $i = e$ or o (even or odd) as

$$\begin{Bmatrix} Y_{nm}^e(\vartheta,\varphi) \\ Y_{nm}^o(\vartheta,\varphi) \end{Bmatrix} = \gamma_{nm} P_n^m(\cos\vartheta) \begin{Bmatrix} \cos m\varphi \\ \sin m\varphi \end{Bmatrix}, \tag{3.11}$$

where

$$\gamma_{nm} = \sqrt{\epsilon_m \frac{2n+1}{4\pi} \frac{(n-m)!}{(n+m)!}} \tag{3.12}$$

with $\epsilon_m = 1$ or 2 for $m = 0$ or $m \ge 1$, respectively, and $P_n^m(\cos\vartheta)$ being associated Legendre polynomials [30]. Spherical harmonics satisfy the orthonormality relations on a spherical surface, thus

$$\begin{aligned} \int_0^{2\pi} \int_0^{\pi} Y_{nm}^i(\vartheta,\varphi) Y_{n'm'}^{i'}(\vartheta,\varphi) \sin\vartheta \, d\vartheta \, d\varphi = \\ = \begin{cases} 1 & \text{if } n = n',\ m = m' = 0,\ i = i' = e, \\ 1 & \text{if } n = n',\ m = m' > 0,\ i = i', \\ 0 & \text{otherwise.} \end{cases} \end{aligned} \tag{3.13}$$

To obtain the TM and TE *radiation modes* we take

$$\underline{A}_r = \underline{F}_r = r Y_{nm}^i(\vartheta,\varphi) h_n^{(2)}(kr) \tag{3.14}$$

in (3.7). The transverse basis one-forms $e_p(\vartheta,\varphi)$ are obtained from (3.9a) and (3.9b) by taking the radius r and frequency ω independent directions

only. Since the magnetic one-form potential $\underline{\mathcal{A}}$ equals to the electric one-form potential $\underline{\mathcal{F}}$, there is a simple relation between the TM and TE radiation modes. The transverse basis one-forms in terms of spherical harmonics are given by

$$e^e_{nmi}(\vartheta,\varphi) = \left(\mathrm{d}\vartheta\frac{\partial}{\partial\vartheta} + \mathrm{d}\varphi\frac{\partial}{\partial\varphi}\right)\frac{Y^i_{nm}(\vartheta,\varphi)}{\sqrt{n(n+1)}}, \tag{3.15a}$$

$$e^h_{nmi}(\vartheta,\varphi) = \perp_n e^e_{nmi}, \tag{3.15b}$$

where the superscripts ^{e} and ^{h} stand for TM(E) and TE(H) radiation modes, respectively.

We conclude that the transverse basis one-forms of the TM radiation modes are given by

$$\begin{Bmatrix}(e^e_{nme})_\vartheta(\vartheta,\varphi)\\(e^e_{nmo})_\vartheta(\vartheta,\varphi)\end{Bmatrix} = c_{nm}(-\sin\vartheta)P^{m\prime}_n(\cos\vartheta)\begin{Bmatrix}\cos m\varphi\\ \sin m\varphi\end{Bmatrix} \tag{3.16a}$$

$$\begin{Bmatrix}(e^e_{nme})_\varphi(\vartheta,\varphi)\\(e^e_{nmo})_\varphi(\vartheta,\varphi)\end{Bmatrix} = c_{nm}mP^m_n(\cos\vartheta)\begin{Bmatrix}-\sin m\varphi\\ \cos m\varphi\end{Bmatrix} \tag{3.16b}$$

with $c_{nm} = \gamma_{nm}/\sqrt{n(n+1)}$ being normalization coefficients which depend on n and m. The prime $'$ denotes derivation of a function with respect to its argument.

The transverse basis one-forms of the TE radiation modes are obtained from (3.16) using (3.15b).

3.2 Cauer Realization of Radiation Modes

Let us assume the complete electromagnetic structure under consideration embedded in a virtual sphere $\mathscr{S}$ as shown in Figure 3.1.

The wave impedances of the TM radiation modes on the surface of the sphere $\mathscr{S}$ are given by

$$\underline{Z}^e_{nm} = j\eta\frac{H^{(2)\prime}_n(kr_0)}{H^{(2)}_n(kr_0)} \tag{3.17}$$

and of the TE radiation modes by

$$\underline{Z}^h_{nm} = -j\eta \frac{H_n^{(2)}(kr_0)}{H_n^{(2)\prime}(kr_0)}, \tag{3.18}$$

where $\eta = \sqrt{\mu/\varepsilon}$ is the wave impedance of the plane wave and $H_n^{(2)}(kr) = krh_n^{(2)}(kr)$. Please note that the characteristic wave impedances depend only on the index n for the given radius r_0 of the virtual sphere.

Using the recurrence formula for the spherical Hankel functions [30], the Cauer representations of the TM and TE radiation modes may be obtained [10], [31]. The impedance of the TM modes is then written as

$$\underline{Z}^e_{nm} = \eta \left\{ \frac{\frac{n}{jkr} + \cfrac{1}{\frac{2n-1}{jkr} + \cfrac{1}{\frac{2n-3}{jkr} + \ddots + \cfrac{1}{\frac{3}{jkr} + \cfrac{1}{\frac{1}{jkr} + 1}}}}}{} \right\}, \tag{3.19a}$$

and of the TE modes as

$$\underline{Z}^h_{nm} = \eta \left\{ \cfrac{1}{\frac{n}{jkr} + \cfrac{1}{\frac{2n-1}{jkr} + \cfrac{1}{\frac{2n-3}{jkr} + \ddots + \cfrac{1}{\frac{3}{jkr} + \cfrac{1}{\frac{1}{jkr} + 1}}}}} \right\}. \tag{3.19b}$$

The equivalent Cauer circuits realizing the impedances of the radiation modes given by (3.19) are shown in Figure 3.4 and Figure 3.5.

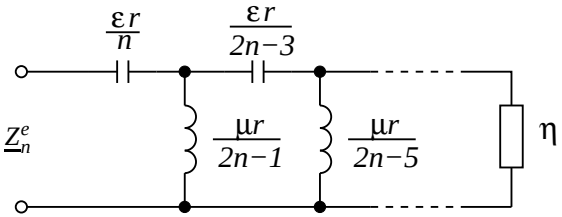

Figure 3.4: Cauer realization of the impedance of TM_n radiation mode.

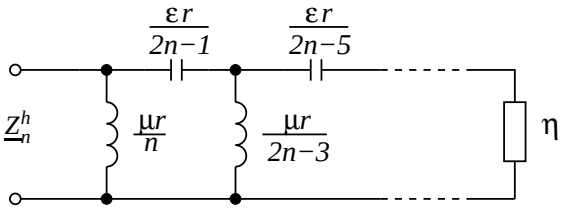

Figure 3.5: Cauer realization of the impedance of TE_n radiation mode.

In Figure 3.6 – Figure 3.9 the plots of real and imaginary parts of the impedances of radiation modes realized by the Cauer circuits and computed analytical by using (3.17) and (3.18) are compared. The plots are shown for both, the TM and TE radiation modes in free-space ($\eta = 377\,\Omega$), and mode numbers $n = 1, 2, 3, 4, 5, 25, 30$.

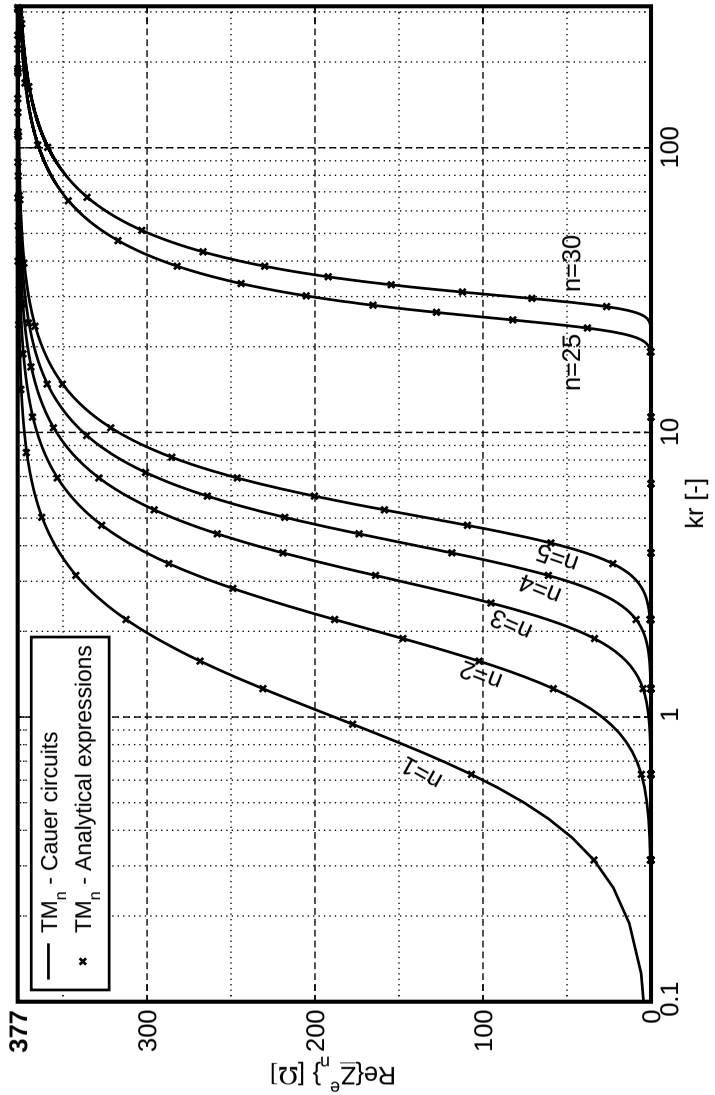

Figure 3.6: TM radiation modes – real part of the impedance.

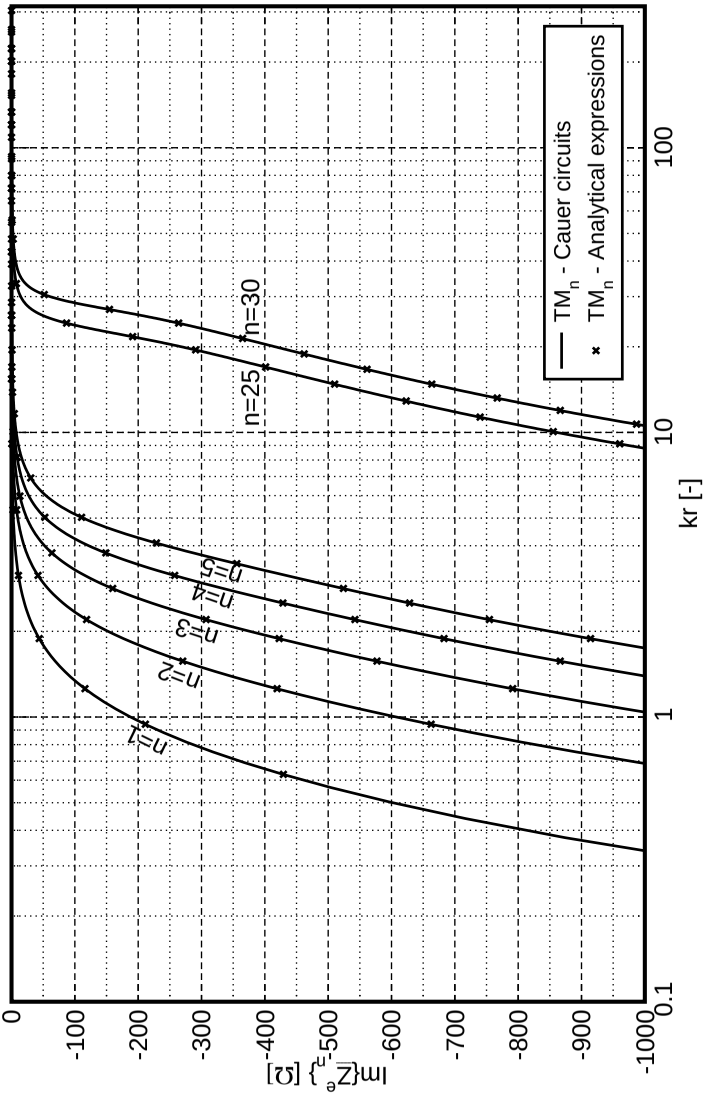

Figure 3.7: TM radiation modes – imaginary part of the impedance.

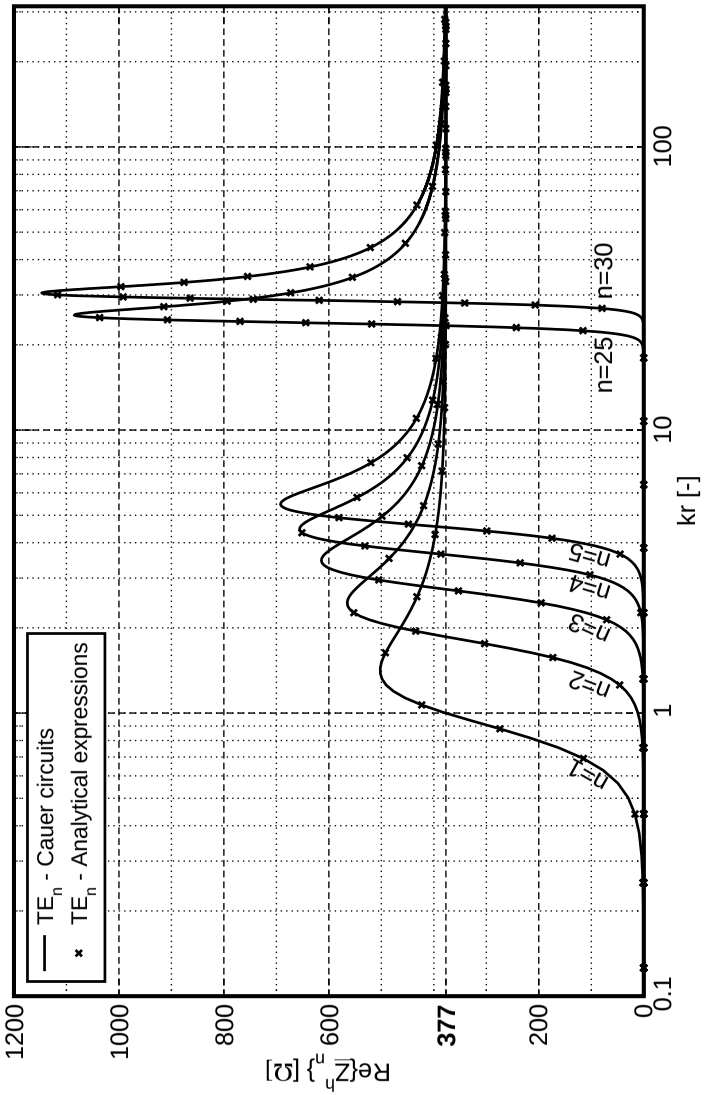

Figure 3.8: TE radiation modes – real part of the impedance.

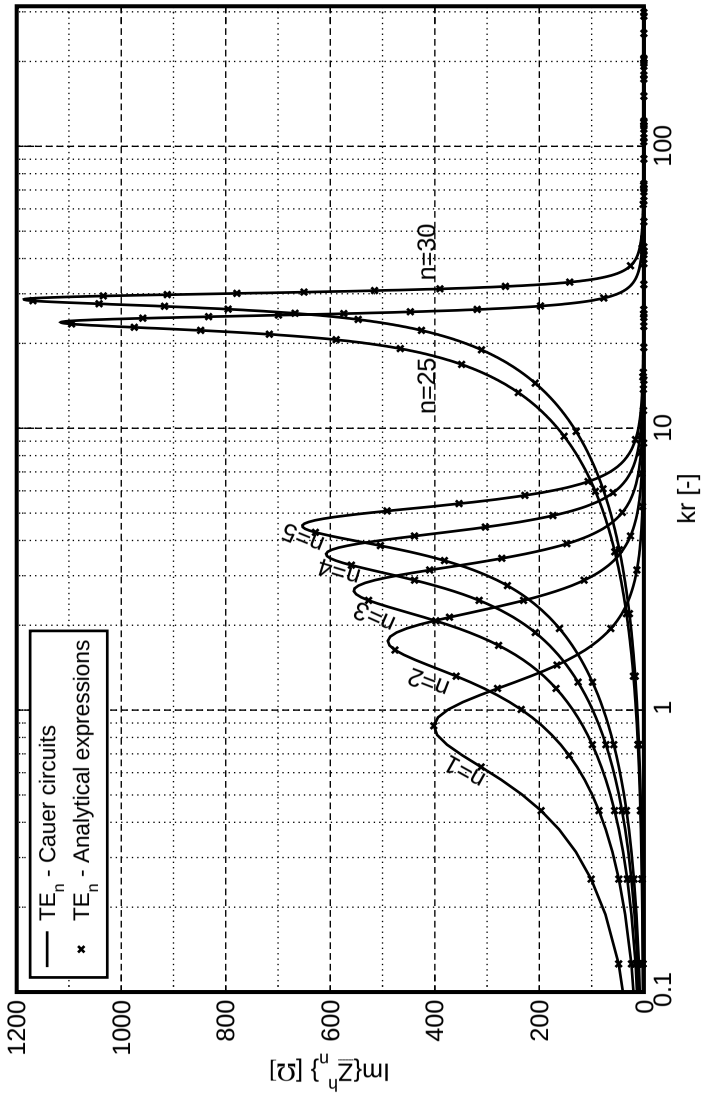

Figure 3.9: TE radiation modes – imaginary part of the impedance.

4 Connection Subnetwork

4.1 Tellegen's Theorem and Connection Subnetwork

Tellegen's theorem is a fundamental theorem in network theory which has been given by Tellegen [32] and generalized by Penfield, Spence and Duinker [33]. Notably, the form of the theorem is simple and general. The beauty and power of the theorem is in it's simplicity and generality.

The importance of the theorem follows from the fact that it's proof depends solely upon Kirchhoff's laws. Consequently, the theorem is valid for all types of networks which satisfy Kirchhoff's laws regardless if these are linear or non-linear, time invariant or time-varying, reciprocal or non-reciprocal, passive or active. The condition which must be satisfied for the theorem to be valid is that the circuits under consideration have common topology.

Since the Tellegen's theorem plays an important role also in the network-oriented modeling, the network form of the theorem will be now given. Then, the field form of the Tellegen's theorem and its discretized form as given in [1] will be described.

4.1.1 Network form of Tellegen's theorem

The Tellegen's theorem states that for two networks sharing the same topology and having B branches the following equation holds

$$\sum_{b=1}^{B} i'_b v''_b = 0, \tag{4.1}$$

where i'_b are branch currents of one network and v''_b are branch voltages of the other network.

The power and usefulness of the theorem can be seen from the two following conclusions, which follow directly from the theorem.

1. If the two networks considered in the formulation of the Tellegen's theorem are the same then (4.1) can be physically interpreted as the conservation of energy principle within the network and has the form

$$\sum_{b=1}^{B} i'_b \, v'_b = 0. \tag{4.2}$$

2. With the previous interpretation of the Tellegen's theorem as energy conservation we can conclude from (4.1) that there does not exist any network which would not conserve energy. In other words, all networks obeying Kirchhoff's laws must conserve energy.

In the generalized form [33] the Tellegen's theorem has the form

$$\sum_{b=1}^{B} \Lambda'(i'_b) \, \Lambda''(v''_b) = 0, \tag{4.3}$$

where Λ' and Λ'' are Kirchhoff current and voltage operators, respectively. Kirchhoff operators, as introduced in [33], are such operators which transform given electrical quantities obeying Kirchhoff's laws into new electrical quantities obeying also Kirchhoff's laws.

Examples of allowed Kirchhoff operators are

- differentiation with respect to time,
- multiplication by a constant,
- any scalar linear transformation.

The proof of the Tellegen's theorem and it's generalized form may be found in [33]. A physical approach to the proof has been given by Temes in [34].

If the sets $\{i'_b\}$ and $\{v''_b\}$ are interpreted as vectors $\mathbf{i}' = \{i'_b\}$ and $\mathbf{v}'' = \{v''_b\}$ then (4.1) can be written as follows

$$\mathbf{i}'^T\mathbf{v}'' = \mathbf{v}''^T\mathbf{i}' = 0. \tag{4.4}$$

This equation can be interpreted as orthogonality relations, i.e., the vectors $\mathbf{i}'$ and $\mathbf{v}''$ are mutually orthogonal.

4.1.2 Field form of Tellegen's theorem

The field form of Tellegen's theorem states that [1], [11]

$$\oint_{\partial V} \mathcal{E}'(\mathbf{x},t') \wedge \mathcal{H}''(\mathbf{x},t'') = 0, \tag{4.5}$$

where $'$ and $''$ denote independent field forms defined on a common manifold ∂V. The theorem states that no energy can be stored inside the manifold ∂V of zero measure.

4.1.3 Connection subnetwork

Scattering matrix of ideal transformer network

The equations of a transformer network as shown in Figure 4.1, with equal reference resistances at the ports, can be summarized in the equation

$$\begin{bmatrix} \mathbf{I} & -\mathbf{N} \\ \mathbf{N}^T & \mathbf{I} \end{bmatrix} \tilde{\mathbf{b}} = \begin{bmatrix} -\mathbf{I} & \mathbf{N} \\ \mathbf{N}^T & \mathbf{I} \end{bmatrix} \tilde{\mathbf{a}} \tag{4.6}$$

with

$$\mathbf{N} = \begin{bmatrix} n_{11} & n_{12} & \dots & n_{1N} \\ n_{21} & n_{22} & \dots & n_{2N} \\ \dots & \dots & \dots & \dots \\ n_{M1} & n_{M2} & \dots & n_{MN} \end{bmatrix} \tag{4.7}$$

summarizing the transformer ratios and

$$\tilde{\mathbf{a}} = \begin{bmatrix} a_{N+1} & a_{N+2} & \dots & a_{N+M} & a_1 & a_2 & \dots & a_N \end{bmatrix}^T, \tag{4.8a}$$

$$\tilde{\mathbf{b}} = \begin{bmatrix} b_{N+1} & b_{N+2} & \dots & b_{N+M} & b_1 & b_2 & \dots & b_N \end{bmatrix}^T \tag{4.8b}$$

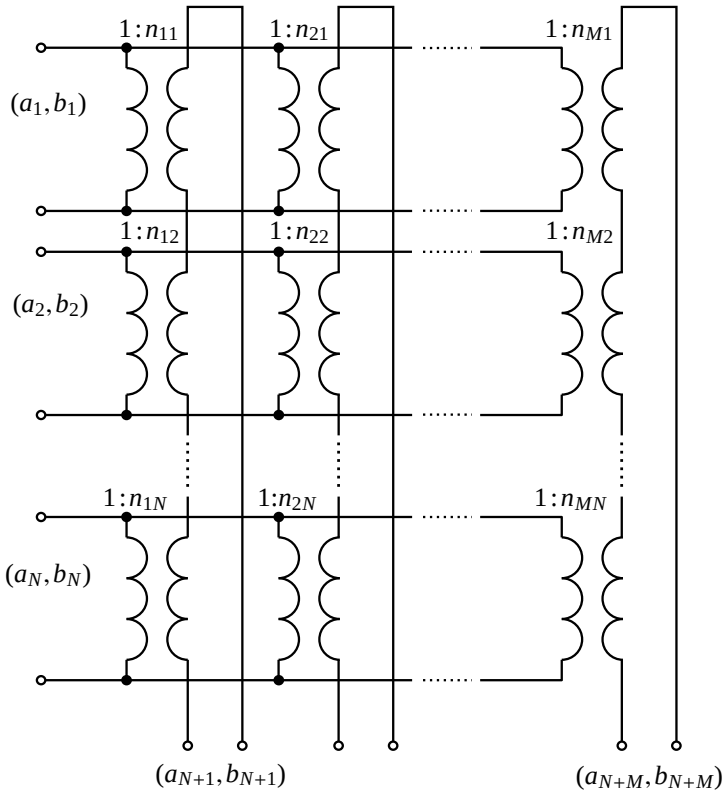

Figure 4.1: Connection subnetwork consisting of ideal transformers.

being the reorganized vectors of incoming and reflected waves.

The reorganized scattering matrix $\tilde{\mathbf{S}}$ is computed as

$$\tilde{\mathbf{S}} = \begin{bmatrix} \mathbf{I} & -\mathbf{N} \\ \mathbf{N}^T & \mathbf{I} \end{bmatrix}^{-1} \begin{bmatrix} -\mathbf{I} & \mathbf{N} \\ \mathbf{N}^T & \mathbf{I} \end{bmatrix} = \begin{bmatrix} \tilde{\mathbf{S}}_4 & \tilde{\mathbf{S}}_3 \\ \tilde{\mathbf{S}}_2 & \tilde{\mathbf{S}}_1 \end{bmatrix}, \tag{4.9}$$

where the inverse matrix can be obtained using the technique of *Schur complement* (see Section A.3.2).

The scattering matrix $\mathbf{S}$ is related to the reorganized scattering matrix $\tilde{\mathbf{S}}$ as follows

$$\mathbf{S} = \begin{bmatrix} \tilde{\mathbf{S}}_1 & \tilde{\mathbf{S}}_2 \\ \tilde{\mathbf{S}}_3 & \tilde{\mathbf{S}}_4 \end{bmatrix}. \tag{4.10}$$

The resulting scattering matrix of the connection subnetwork is given as

$$\mathbf{S} = \begin{bmatrix} \mathbf{I} - 2\mathbf{N}^T\mathbf{S}_A^{-1}\mathbf{N} & \mathbf{N}^T\mathbf{S}_A^{-1} + \mathbf{N}^T - \mathbf{N}^T\mathbf{S}_A^{-1}\mathbf{N}\mathbf{N}^T \\ 2\mathbf{S}_A^{-1}\mathbf{N} & -\mathbf{S}_A^{-1} + \mathbf{S}_A^{-1}\mathbf{N}\mathbf{N}^T \end{bmatrix}, \tag{4.11}$$

with

$$\mathbf{S}_A = \mathbf{I} + \mathbf{N}\mathbf{N}^T, \tag{4.12}$$

where $\mathbf{S}_A$ is the Schur complement.

Examples

In the following let us examine some special cases of the scattering matrix (4.11).

Orthonormal square N

In this case

$$\mathbf{N}\mathbf{N}^T = \mathbf{N}^T\mathbf{N} = \mathbf{I} \tag{4.13}$$

and

$$\mathbf{S}_A = 2\mathbf{I}; \qquad \mathbf{S}_A^{-1} = \frac{1}{2}\mathbf{I}. \tag{4.14}$$

The (4.11) is simplified to

$$\mathbf{S} = \begin{bmatrix} \mathbf{0} & \mathbf{N}^T \\ \mathbf{N} & \mathbf{0} \end{bmatrix} \tag{4.15}$$

$\mathbf{N}^T$ is a right inverse of $\mathbf{N}$

In this case

$$\mathbf{N}\mathbf{N}^T = \mathbf{I} \tag{4.16}$$

but

$$\mathbf{N}^T\mathbf{N} \neq \mathbf{I} \tag{4.17}$$

The

$$\mathbf{S}_A = 2\mathbf{I}; \qquad \mathbf{S}_A^{-1} = \frac{1}{2}\mathbf{I}. \tag{4.18}$$

The (4.11) is simplified to

$$\mathbf{S} = \begin{bmatrix} \mathbf{I} - \mathbf{N}^T\mathbf{N} & \mathbf{N}^T \\ \mathbf{N} & \mathbf{0} \end{bmatrix} \tag{4.19}$$

Ideal transformer: N-ports primary, one-port secondary

The transformer ratios are denoted by n_i with $i = 1, \ldots, N$. The matrix $\mathbf{N}$ is reduced to a vector

$$\mathbf{N} = \begin{bmatrix} n_1 & n_2 & \ldots & n_N \end{bmatrix} \tag{4.20}$$

The $(N+1)\times(N+1)$ S-matrix is given by

$$\mathbf{S} = D \begin{bmatrix} \frac{1}{D} + n_1^2 & n_1 n_2 & n_1 n_3 & \ldots & n_1 n_N & -n_1 \\ n_2 n_1 & \frac{1}{D} + n_2^2 & n_2 n_3 & \ldots & n_2 n_N & -n_2 \\ \vdots & \vdots & \vdots & \vdots & \vdots & \vdots \\ n_N n_1 & n_N n_2 & n_N n_3 & \ldots & \frac{1}{D} + n_N^2 & -n_N \\ -n_1 & -n_2 & -n_3 & \ldots & -n_N & \frac{1}{D} + 1 \end{bmatrix} \tag{4.21a}$$

with

$$D = -\frac{2}{1 + n_1^2 + \ldots + n_N^2}. \tag{4.21b}$$

Note that if $n_1^2 + \ldots + n_N^2 = 1$ then $D = -1$ and the scattering matrix has a zero at the last element.

For the special case of $N = 1$, the scattering matrix computed from (4.21) is reduced to

$$\mathbf{S} = \frac{1}{1+n_1^2}\begin{bmatrix} 1-n_1^2 & 2n_1 \\ 2n_1 & n_1^2-1 \end{bmatrix}, \tag{4.22}$$

which may be found in the literature (e.g., see [35] p.41).

4.2 Scattering Matrix of the Connection Subnetwork

4.2.1 Direct derivation

Boundary conditions

In the following, the TLM simulation domain ($\mathscr{R}_1$) will be referred to as subdomain 1 and the outside space ($\mathscr{R}_2$) as subdomain 2. The two subdomains are identified by a spherical surface ($\mathscr{S}$) between the two (see also Figure 1.1). Also, it will be convenient to use the vector notation for electromagnetic fields in this Section.

First, the tangential electric field on the interfacing surface (i.e. on the sphere) is expanded into two sets of vector basis functions $\mathbf{e}_n^{(1)}$ and $\mathbf{e}_m^{(2)}$ with indices $n = 1, 2, \ldots, N$ and $m = 1, 2, \ldots, M$. The electric fields can be written as

$$\mathbf{E}_t^{(1)} = \sum_n^N V_n^{(1)} \mathbf{e}_n^{(1)}, \tag{4.23a}$$

$$\mathbf{E}_t^{(2)} = \sum_m^M V_m^{(2)} \mathbf{e}_m^{(2)}, \tag{4.23b}$$

with superscripts $^{(1)}$ and $^{(2)}$ denoting the subdomain 1 and 2, respectively. We call the modal amplitudes $V_n^{(1)}$ and $V_m^{(2)}$ *equivalent voltages*.

Considering equality of the tangential fields represented by (4.23) we can write

$$\mathbf{E}_t^{(1)} = \mathbf{E}_t^{(2)}. \tag{4.24}$$

Multiplying both sides of the equation with $\mathbf{e}^{(2)}$ and integrating over $\mathscr{S}$ we get

$$\int_{\mathscr{S}} \sum_{n}^{N} V_n^{(1)} \mathbf{e}_n^{(1)} \cdot \mathbf{e}_m^{(2)} \, \mathrm{d}\mathscr{S} = \int_{\mathscr{S}} \sum_{m'}^{M} V_{m'}^{(2)} \mathbf{e}_{m'}^{(2)} \cdot \mathbf{e}_m^{(2)} \, \mathrm{d}\mathscr{S}, \tag{4.25a}$$

where $\mathscr{S}$ denotes the domain of integration, here the spherical surface between subdomain 1 and 2. Assuming orthonormality of the basis functions (4.25a) results in

$$V_m^{(2)} = \sum_{n}^{N} V_n^{(1)} \int_{\mathscr{S}} \mathbf{e}_n^{(1)} \cdot \mathbf{e}_m^{(2)} \, \mathrm{d}\mathscr{S}. \tag{4.25b}$$

The tangential magnetic fields in the subdomain 2 are related to the tangential electric fields in the same subdomain via

$$\mathbf{H}_t^{(2)} = \sum_{m}^{M} I_m^{(2)} \mathbf{r}_0 \times \mathbf{e}_m^{(2)}, \tag{4.26a}$$

with

$$I_m^{(2)} = \frac{V_m^{(2)}}{Z_m^{(2)}} = Y_m^{(2)} V_m^{(2)}, \tag{4.26b}$$

where $Z_m^{(2)}$ and $Y_m^{(2)}$ are *equivalent impedances* and *equivalent admittances* of the m-th radiation mode. The quantities $I_m^{(2)}$ and $I_n^{(1)}$ are called *equivalent currents*.

Similar considerations may be done for the tangential magnetic fields resulting in an equation analogous to (4.25b). The equation relates the equivalent currents in domain 1 to those in domain 2 and reads

$$I_n^{(1)} = \left(-1\right) \sum_{m}^{M} I_m^{(2)} \int_{\mathscr{S}} \mathbf{e}_m^{(2)} \cdot \mathbf{e}_n^{(1)} \, \mathrm{d}\mathscr{S}. \tag{4.27}$$

Next, we define the coefficient n_{mn} by

$$n_{mn} = \int_{\mathscr{S}} \mathbf{e}_m^{(2)} \cdot \mathbf{e}_n^{(1)} \, \mathrm{d}\mathscr{S} \tag{4.28}$$

and the matrix $\mathbf{N}$ as

$$\mathbf{N} = \begin{bmatrix} n_{11} & n_{12} & \dots & n_{1N} \\ n_{21} & n_{22} & \dots & n_{2N} \\ \dots & \dots & \dots & \dots \\ n_{M1} & n_{M2} & \dots & n_{MN} \end{bmatrix}. \tag{4.29}$$

Mapping between network quantities and wave quantities

The equivalent voltages and equivalent currents in subdomain 1 are transformed to the wave quantities by

$$V_n^{(1)} = a_n^{(1)} + b_n^{(1)}, \tag{4.30a}$$

$$\eta I_n^{(1)} = a_n^{(1)} - b_n^{(1)}, \tag{4.30b}$$

where $a_n^{(1)}$ and $b_n^{(1)}$ are the amplitudes of the incoming and outgoing waves with respect to the surface of the sphere and where $\eta = \sqrt{\mu/\varepsilon}$.

On the boundary of subdomain 2 we introduce local incoming waves $a_m^{(2)}$ and local reflected waves $b_m^{(2)}$ in a similar manner. The equivalent voltages and currents are related to the wave quantities by

$$V_m^{(2)} = a_m^{(2)} + b_m^{(2)}, \tag{4.31a}$$

$$\eta I_m^{(2)} = a_m^{(2)} - b_m^{(2)}. \tag{4.31b}$$

The Scattering Matrix

Inserting (4.30) and (4.31) into (4.25b) and (4.27) and with (4.28) we obtain the equations of the connection subnetwork between the two subdo-

mains

$$a_m^{(2)} = \left[\sum_n^N \left(a_n^{(1)} + b_n^{(1)}\right) n_{mn}\right] - b_m^{(2)}, \tag{4.32a}$$

$$a_n^{(1)} = b_n^{(1)} - \left[\sum_m^M \left(a_m^{(2)} - b_m^{(2)}\right) n_{mn}\right]. \tag{4.32b}$$

Equations (4.32) can be rewritten as

$$b_m^{(2)} - \sum_n^N b_n^{(1)} n_{mn} = -a_m^{(2)} + \sum_n^N a_n^{(1)} n_{mn}, \tag{4.33a}$$

$$b_n^{(1)} + \sum_m^M b_m^{(2)} n_{mn} = a_n^{(1)} + \sum_m^M a_m^{(2)} n_{mn}. \tag{4.33b}$$

Using matrix notation, the left hand side of equations (4.33) can be written as

$$\begin{bmatrix} -n_{11} & -n_{12} & \dots & -n_{1N} & 1 & 0 & \dots & 0 \\ -n_{21} & -n_{22} & \dots & -n_{2N} & 0 & 1 & \dots & 0 \\ \dots & \dots & \dots & \dots & \dots & \dots & \dots & \dots \\ -n_{M1} & -n_{M2} & \dots & -n_{MN} & 0 & 0 & \dots & 1 \\ 1 & 0 & \dots & 0 & n_{11} & n_{21} & \dots & n_{M1} \\ 0 & 1 & \dots & 0 & n_{12} & n_{22} & \dots & n_{M2} \\ \dots & \dots & \dots & \dots & \dots & \dots & \dots & \dots \\ 0 & 0 & \dots & 1 & n_{1N} & n_{2N} & \dots & n_{MN} \end{bmatrix} \begin{bmatrix} b_1^{(1)} \\ b_2^{(1)} \\ \vdots \\ b_N^{(1)} \\ b_1^{(2)} \\ b_2^{(2)} \\ \vdots \\ b_M^{(2)} \end{bmatrix}, \tag{4.34a}$$

which can be written in short form using block matrix **B** as

$$\begin{bmatrix} -\mathbf{N} & \mathbf{I} \\ \mathbf{I} & \mathbf{N}^T \end{bmatrix} \mathbf{b} = \mathbf{B}\mathbf{b}, \tag{4.34b}$$

where **b** is the vector of outgoing waves.

In a similar way we can write the right hand side of equations (4.33) as

$$\begin{bmatrix} n_{11} & n_{12} & \dots & n_{1N} & -1 & 0 & \dots & 0 \\ n_{21} & n_{22} & \dots & n_{2N} & 0 & -1 & \dots & 0 \\ \dots & \dots & \dots & \dots & \dots & \dots & \dots & \dots \\ n_{M1} & n_{M2} & \dots & n_{MN} & 0 & 0 & \dots & -1 \\ 1 & 0 & \dots & 0 & n_{11} & n_{21} & \dots & n_{M1} \\ 0 & 1 & \dots & 0 & n_{12} & n_{22} & \dots & n_{M2} \\ \dots & \dots & \dots & \dots & \dots & \dots & \dots & \dots \\ 0 & 0 & \dots & 1 & n_{1N} & n_{2N} & \dots & n_{MN} \end{bmatrix} \begin{bmatrix} a_1^{(1)} \\ a_2^{(1)} \\ \vdots \\ a_N^{(1)} \\ a_1^{(2)} \\ a_2^{(2)} \\ \vdots \\ a_M^{(2)} \end{bmatrix}, \tag{4.35a}$$

which can be written in short form using block matrix **A** as

$$\begin{bmatrix} \mathbf{N} & -\mathbf{I} \\ \mathbf{I} & \mathbf{N}^T \end{bmatrix} \mathbf{a} = \mathbf{A}\mathbf{a}, \tag{4.35b}$$

where **a** is the vector of incoming waves.

Equation (4.34b) must be equal to (4.35b) by (4.33). Taking the inverse matrix $\mathbf{B}^{-1}$ we obtain

$$\mathbf{b} = \mathbf{B}^{-1}\mathbf{A}\,\mathbf{a} = \mathbf{S}\,\mathbf{a}, \tag{4.36}$$

where **S** is the scattering matrix of the connection between subdomain 1 and 2.

Reorganizing the vectors of incoming and outgoing waves according to

$$\tilde{\mathbf{a}} = \begin{bmatrix} a_1^{(2)} & a_2^{(2)} & \dots & a_M^{(2)} & a_1^{(1)} & a_2^{(1)} & \dots & a_N^{(1)} \end{bmatrix}^T, \tag{4.37a}$$

$$\tilde{\mathbf{b}} = \begin{bmatrix} b_1^{(2)} & b_2^{(2)} & \dots & b_M^{(2)} & b_1^{(1)} & b_2^{(1)} & \dots & b_N^{(1)} \end{bmatrix}^T, \tag{4.37b}$$

equations (4.34b) and (4.35b) take the same form as the equation (4.6). This shows that the transformation ratios of the connection subnetwork in (4.7) are to be taken according to (4.28).

Discretized electromagnetic field

When the electromagnetic field functions are discretized in space, the equality (4.24) cannot be satisfied, unless the basis functions in both subdomains

form a complete set and the summations are taken over all basis functions. However, pointwise equality for the sampled field functions can be satisfied.

Consider a set of points $\mathscr{R}_{\mathscr{S}}$, elements of which are all discrete points on the surface of the spherical domain, i.e., $\mathbf{r}_s \in \mathscr{R}_{\mathscr{S}}$. Index s denotes a particular point on the surface. Using the sampling property of the Dirac delta function we can write

$$\mathsf{E}^{(1)}(\mathbf{r}_s) = \sqrt{\Delta A(\mathbf{r}_s)} \int_{\mathscr{S}} \mathbf{E}_t^{(1)}(\mathbf{r}) \delta(\mathbf{r} - \mathbf{r}_s) \, \mathrm{d}\mathscr{S}, \tag{4.38}$$

where we leave out the subscript t for discretized tangential fields and where

$$\Delta A(\mathbf{r}_s) = \Delta A_s = \int_{\mathscr{V}(\mathbf{r}_s)} \mathrm{d}\mathscr{S}. \tag{4.39}$$

The domain $\mathscr{V}(\mathbf{r}_s)$ is the Voronoi region around point $\mathbf{r}_s$. Furthermore,

$$\int_{\mathscr{S}} \mathrm{d}\mathscr{S} \approx \sum_{s}^{S} \Delta A_s = 4\pi. \tag{4.40}$$

With

$$\mathsf{E}_s = \mathsf{E}(\mathbf{r}_s) \tag{4.41}$$

we can define the vector

$$\mathbf{E} = \left\{ \mathsf{E}_1, \mathsf{E}_2, \ldots, \mathsf{E}_S \right\}^T. \tag{4.42}$$

The equality (4.24) can be satisfied now and reads

$$\mathbf{E}^{(1)} = \mathbf{E}^{(2)}. \tag{4.43}$$

4.2.2 Implementation Issues

The number of elements to be stored for any S-matrix of the permissible connection network:

$$\text{elements} = \frac{N(N+1)}{2}, \tag{4.44}$$

since the matrix is symmetric.

The memory requirements to store the scattering matrix are following:

$$\text{memory} = \frac{64}{8}\frac{1}{1024\times 1024\times 1024}\times \text{elements} \approx 7.45\times 10^{-9}\times \frac{N(N+1)}{2}\,[\text{GB}]. \tag{4.45}$$

A $10\,000\times 10\,000$ matrix requires cca 382 MB of memory.

5 Transmission Line Matrix – Multipole Expansion Method

In this Chapter we use the results obtained in previous chapters as a basis for the hybrid Transmission Line Matrix – Multipole Expansion (TLMME) method. Individual parts of the hybrid TLMME method will be described in detail.

We begin with the description of a spherical TLM region. Then, the pre-processing part of the TLMME method is given. During pre-processing the spherical TLM region is generated, a scattering matrix of the connection subnetwork is computed and Wave Digital Filter (WDF) models of impedances of radiation modes are created. We will see how these filters are implemented and synchronized with the TLM method.

The processes of generation of the spherical TLM region, meshing of geometric objects and creation of recursive WDF models of impedances of radiation modes have been fully automatized. This avoids errors introduced by manual pre-processing and enables fast pre-processing of technically interesting models.

The Chapter is concluded with the description of the TLMME algorithm.

5.1 Spherical TLM Region

Since the transverse basis one-forms $e_p(\vartheta,\varphi)$ in (3.15) are defined on the surface of a spherical manifold, we cannot simply proceed with the connection of the classical cubical TLM simulation domain to the radiation modes.

Therefore, we embed the TLM simulation domain into a sphere, which is discretized in a rectangular mesh, and obtain a spherical TLM region

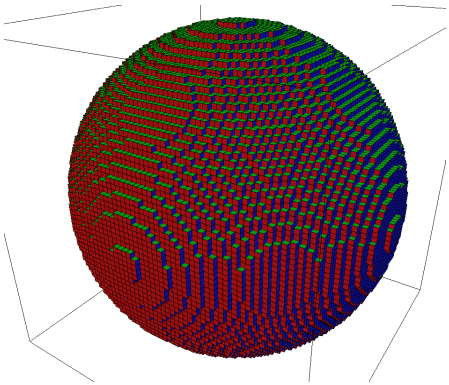

Figure 5.1: The spherical TLM region – discretized spherical manifold $\mathscr{S}$.

bounded by a discretized spherical manifold $\mathscr{S}$ as depicted in Figure 5.1.

Inside the spherical TLM region the electromagnetic field is modeled by TLM. On the boundary of the spherical domain – on the discretized spherical manifold $\mathscr{S}$ – we define a set of surfaces on which the fields resulting from the TLM algorithm are obtained. This set will be denoted by $\mathscr{S}^C$ and its elements (surfaces) by $s^c \in \mathscr{S}^C$. The fields on s^c are used to compute the modal coefficients in (5.2).

5.1.1 Connection of the simulation domain to the radiation modes

The transverse field one-forms are expressed as a linear combinations of the basis one-forms by

$$\mathcal{N}_t(r,\vartheta,\varphi,t)\Big|_{r=r_0} = \sum_{n,m,i,s} \alpha^s_{nmi}(t)\mathfrak{s}^s_{nmi}(\vartheta,\varphi), \tag{5.1}$$

where the index $s = e$ or h stands for TM(E) or TE(H) modes, respectively, and s stands for the basis structure one-forms e or h as defined in (3.1). In (5.1) $\mathcal{N}$ stands for the one-form fields $\mathcal{E}$ or $\mathcal{H}$.

Using the orthonormal property of the structure one-forms, the time-dependent modal coefficients $\alpha^s_{nmi}(t)$ are given by

$$\alpha^s_{nmi}(t) = \int_0^{2\pi}\int_0^{\pi} \left(-\perp_n \mathcal{N}(r,\vartheta,\varphi,t)\Big|_{r=r_0} \right) \wedge s^s_{nmi}(\vartheta,\varphi). \tag{5.2}$$

For simplicity of the notation, let us consider in the following just one mode with given n, m, i, s.

We may write the structure one-forms in (5.2) as

$$s = s_\vartheta m_\vartheta \,\mathrm{d}\vartheta + s_\varphi m_\varphi \,\mathrm{d}\varphi, \tag{5.3}$$

with m_ϑ and m_φ being the metric coefficients of the spherical manifold.

On each surface s^c of the discretized manifold of $\mathscr{S}(r)$ we have knowledge of $N_x(x,y,z,t)$, $N_y(x,y,z,t)$ or $N_z(x,y,z,t)$. After projecting these field values onto the spherical manifold $\mathscr{S}(r)$, we can write (5.2) as

$$\begin{aligned} \alpha(t) = \int_0^{2\pi}\int_0^{\pi} \{ & N_x(\vartheta,\varphi,t)\left[t_{12}s_\vartheta m_\vartheta + t_{13}s_\varphi m_\varphi\right] + \\ & + N_y(\vartheta,\varphi,t)\left[t_{22}s_\vartheta m_\vartheta + t_{23}s_\varphi m_\varphi\right] + \\ & + N_z(\vartheta,\varphi,t)\left[t_{32}s_\vartheta m_\vartheta + t_{33}s_\varphi m_\varphi\right]\} \,\mathrm{d}\vartheta \wedge \mathrm{d}\varphi, \end{aligned} \tag{5.4}$$

with $t_{12} = \partial x/\partial\vartheta$, $t_{13} = \partial x/\partial\varphi$, $t_{22} = \partial y/\partial\vartheta$, $t_{23} = \partial y/\partial\varphi$, $t_{32} = \partial z/\partial\vartheta$ and $t_{33} = \partial z/\partial\varphi$. For the considered spherical manifold the metric coefficients are $m_\vartheta = 1$ and $m_\varphi = \sin\vartheta$.

Using the point-matching technique, the time-dependent modal coefficients can be computed numerically by

$$\alpha(t) = \int_0^{2\pi}\int_0^{\pi} [S\,P_x + S\,P_y + S\,P_z] \sin\vartheta \, d\vartheta \, d\varphi = \int_0^{2\pi}\int_0^{\pi} S\,P \sin\vartheta \, d\vartheta \, d\varphi, \tag{5.5}$$

with

$$S\,P_x = N_x(\vartheta,\varphi,t)\left[t_{12}s_\vartheta + t_{13}s_\varphi\right], \tag{5.6a}$$

$$S\,P_y = N_y(\vartheta,\varphi,t)\left[t_{22}s_\vartheta + t_{23}s_\varphi\right], \tag{5.6b}$$

$$S\,P_z = N_z(\vartheta,\varphi,t)\left[t_{32}s_\vartheta + t_{33}s_\varphi\right]. \tag{5.6c}$$

The integral in (5.5) is obtained numerically as

$$\alpha(t) \approx \sum_{\vartheta_d} \sum_{\varphi_d} S\, P(\vartheta_d, \varphi_d, t) \sin\vartheta_d\, \Delta_{\vartheta_d}\, \Delta_{\varphi_d}, \tag{5.7}$$

with

$$\sum_{\vartheta_d} \Delta_{\vartheta_d} = \pi, \quad \sum_{\varphi_d} \Delta_{\varphi_d} = 2\pi. \tag{5.8}$$

In (5.7), ϑ_d and φ_d are the discrete elevation and azimuth, respectively, at the points where the fields of the surface element s^c are defined, and Δ_{ϑ_d} and Δ_{φ_d} are the spatial discretization steps in the corresponding direction, which differ with the location of the element s^c.

The modal coefficients in (5.7) represent the input of the corresponding radiation mode. Each TLM port of the surface element s^c contributes to the total radiation. The lumped element equivalent circuit model of the connection circuit connecting the TLM network representing the simulation domain with the ladder networks representing the radiation modes is shown in Figure 5.2. In [1] it has been shown, that the connection network contains only ideal transformers.

5.2 Pre-processing

Pre-processing for the TLMME method consists of the following steps:

1. Generation of the spherical TLM region,
2. computation of the scattering matrix of the connection subnetwork,
3. creation of the WDF models of radiation modes,
4. meshing of the physical objects in the TLM method,
5. generation of the models of excitation.

The generation of the spherical TLM region is done automatically using a Cartesian mesh generator which is described in the next Section.

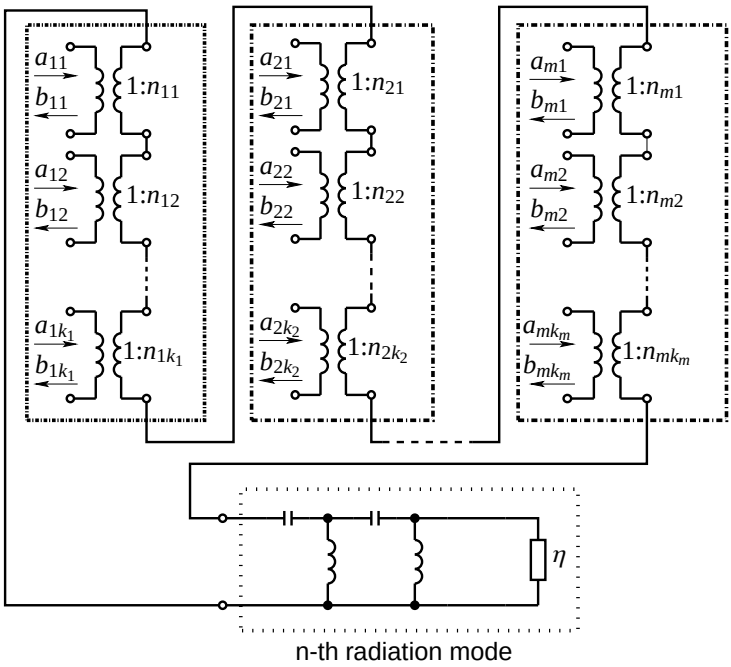

Figure 5.2: Network model of the connection of one radiation mode to the TLM simulation domain.

WDF models of the impedances of radiation modes are also generated automatically by taking advantage of their recursive structure. More details are given in Section 5.2.2.

5.2.1 Cartesian mesh generation

The discretization procedure we are using here is an extension of the method described in [36] for 2D manifolds. The discretization of 2D closed manifolds follows these steps:

1. create a model of the 2D manifold,
2. define the mesh,
3. discretize the object using *ray shooting* technique,
4. extract the boundary from the volumetric object.

This method works for volumetric objects which exhibit a closed boundary. However, using boolean operations the method may be extended to discretize non-closed general 2D objects.

The principles of the ray shooting technique are shown in Figure 5.3. A ray with two constant spatial coordinates is examined for the intersections with the object under consideration. Since we know that the object has a closed boundary, i.e., it is a finite volume object, we identify the object in the prescribed mesh. Now, the boundary of the discretized volumetric object may be easily extracted. As a result we get the 2D discretized manifold. This manifold may be represented by a set of elementary surfaces, e.g., by $\mathscr{S}^C$ defined in Section 5.1.

Example: Cartesian meshing of a rectangular cavity resonator

The 3D Transmission Line Matrix (TLM) method has been originally developed in a structured Cartesian mesh [13], [26], [11]. The formulation of the TLM algorithm in structured Cartesian mesh is the easiest one and the implementation is straightforward. However, the lack of conformity of

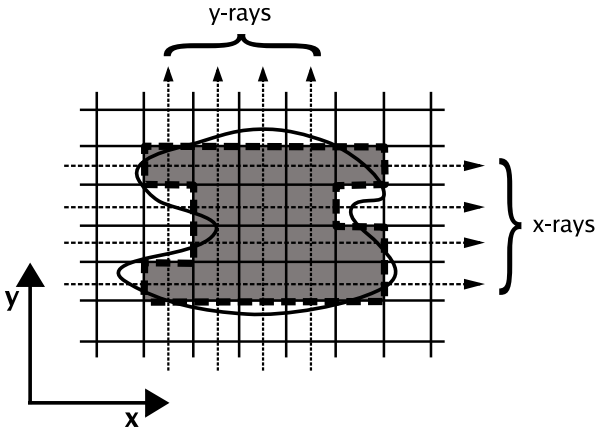

Figure 5.3: The ray shooting technique.

the Cartesian mesh to the boundaries of complex curved objects has been soon recognized.

Researchers have tried to improve the conformity of the mesh to the boundaries of the objects by using graded, conformal, unstructured triangular and tetrahedral meshes [37]. However, all of these approaches increase the complexity of the TLM computation. Higher memory requirements, mesh queries and additional specialized techniques increase the complexity of the TLM algorithm and computational time.

Another very important aspect is the possibility of parallelization of the TLM solver. Structured solvers are much easier to be parallelized then unstructured solvers. In general, properly designed structured solvers are also always faster and more robust than properly designed unstructured solvers.

Obviously, the main arguments why to use unstructured solvers is the conformity of the mesh to the object and easier mesh generation than for a structured solver. On the other hand, if we are able to approximate complex curved geometries within a high-resolution structured Cartesian mesh, i.e., a mesh where the spatial resolution is much higher than the curvature

of the object, the computed solution will converge to the solution computed with an unstructured mesh. A study on the influence of the stepped (staircase) boundaries has been done for the finite-difference time-domain method in [38].

Since TLM in the formulation of Symmetrical Condensed Node (SCN) (and all the other condensed nodes) has both the electric field components and the magnetic field components defined at the same discrete spatial coordinate, it is easy to introduce boundary conditions in the face of the TLM cell. We may use the surfaces available from the TLM mesh to approximate the curved two-dimensional objects. If the structured mesh has a sufficient resolution, the curvature of the objects is well approximated.

In this example we use a regular structured Cartesian mesh with a high spatial resolution – a High-Resolution Mesh (HRM). An HRM is capable of approximating curved objects with high accuracy, since the spatial discretization step is much smaller then the curvature of the object. The rectangular waveguide is discretized within this mesh. Due to the relative ease of parallelization a parallel computational environment is also used.

An off-grid perfect boundary condition for the FDTD method has been published by Rickard and Nikolova [39], implementing an enhanced staircase approximations. We use the same rectangular resonator as in the above mentioned paper and compare the results obtained in the HRM.

The rectangular cavity resonator has dimensions $a = 10$ mm, $b = 20$ mm, $l = 30$ mm, with the l-th dimension located along the z axis. The resonator is rotated in the ϑ and φ directions and discretized using the HRM.

The configuration of the simulation and the simulation times are summarized in Table 5.1 and Table 5.2, respectively. The calculated resonant frequencies and the relative error are summarized in Table 5.3. For the simulations computing nodes with Pentium4 3.0 GHz processors, 1GB 400 DDR memory, connected with 1-Gbit/s switched Ethernet network, have been used.

5.2.2 Wave Digital Filter models of radiation modes

We have seen in Section 3.2 the equivalent Cauer canonical representations of impedances of TE and TM radiation modes. In this Section these

ϑ	φ	Δl	# Cells
0°	0°	1 mm	$28 \times 18 \times 38 = 19152$
45°	0°	1 mm	$40 \times 18 \times 40 = 28800$
45°	0°	0.5 mm	$76 \times 32 \times 76 = 184832$
45°	0°	0.25 mm	$156 \times 52 \times 156 \doteq 1.265 \times 10^6$
45°	45°	0.25 mm	$156 \times 148 \times 156 \doteq 3.4 \times 10^6$
45°	45°	0.125 mm	$300 \times 284 \times 284 \doteq 24.2 \times 10^6$

Table 5.1: Configuration of the rectangular cavity resonator. The distribution ratio in the distributed case is given in the brackets ($x : y : z$).

ϑ	φ	Δl [mm]	t standalone	t distributed
0°	0°	1 mm	1.43 min	-
45°	0°	1 mm	2.03 min	-
45°	0°	0.5 mm	9.72 min	-
45°	0°	0.25 mm	2.5 h	40.43 min; (2:3:1)
45°	45°	0.25 mm	6.5 h	1.82 h; (2:3:1)
45°	45°	0.125 mm	-	21.78 h; (7:1:1)

Table 5.2: Simulation times of the rectangular cavity resonator.

ϑ	φ	Δl [mm]	f_{011}; δ[%]	f_{012}; δ[%]	f_{101}; δ[%]
0°	0°	1	9.0101; 0.027	12.493; 0.012	15.805; 0.029
45°	0°	1	8.8223; 2.057	12.228; 2.107	15.556; 1.547
45°	0°	0.5	8.9624; 0.5	12.45; 0.331	15.705; 0.604
45°	0°	0.25	9.027; 0.215	12.537; 0.365	15.77; 0.192
45°	45°	0.25	8.973; 0.385	12.434; 0.4599	15.717; 0.528
45°	45°	0.125	9.0002; 0.082	12.479; 0.099	15.7811; 0.122

Table 5.3: Calculated resonant frequencies of the rectangular cavity resonator. All frequencies are given in GHz. Next to the resonant frequency the relative error is given.

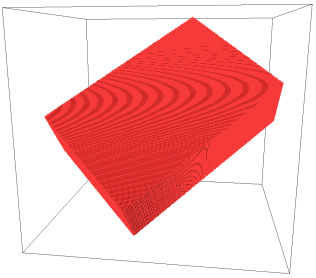

Figure 5.4: Rectangular cavity resonator discretized with HRM; $\vartheta = 45°$, $\varphi = 45°$, $\Delta l = 0.125$ mm.

impedance representations will be transformed into their equivalent digital counterparts using Wave Digital Filters (WDFs) [25].

One main advantage of using WDFs over discrete filter structures obtained via other transformation techniques like direct bilinear transform or impulse invariance is their usage of wave quantities as port signals. This is a considerable advantage for the TLM method which is also based on wave quantities.

With WDFs we can directly realize in digital domains the digital counterparts of analog circuit elements like capacitors, inductors, resistors and interconnections. Also, it is not difficult to generate ladder structures recursively. Since the equivalent representations of radiation modes are ladder structures, they can be efficiently generated using these techniques.

Capacitors, inductors, resistors and interconnections as WDFs

The behaviour of capacitors, inductors, resistors and interconnections can be efficiently and elegantly transformed to digital domain with WDFs (see [25], pp. 274–280).

A capacitor is implemented as a time-delay by one time step with refer-

ence port resistance R_C. The port resistance R_C is given by

$$R_C = \frac{1}{C}\frac{\Delta t}{2}, \tag{5.9}$$

where C is the capacitance of the analog capacitor to be modeled and Δt is the discrete time step of the digital system. For our purposes Δt is equal to the time step of the TLM algorithm.

Similarly, an inductor is implemented as a time-delay by one time step with reference port resistance R_L. The port resistance R_L is given by

$$R_L = L\frac{2}{\Delta t}, \tag{5.10}$$

where L is the inductance of the analog inductor to be modeled.

Notably, the WDF realizations of capacitors and inductors lead to the same results as those obtained from transmission line considerations by Christopoulos (see [26], pp. 25–38).

The port resistance of a resistor is chosen to equal the resistance of the analog resistor. Consequently, a resistor can be easily modeled as an element without any reflection.

For the modeling of interconnection networks we use the parallel and series adaptors. The port resistances of the interconnection network can be chosen independently. The scattering matrices of the adaptors are delay-free and energy conservative.

Recursive generation of ladder structures

For the recursive generation of WDF ladder structures the *realizability* condition is important. Realizability is granted when no delay-free directed loop exists in the signal-flow diagram of the WDF and if the total delay in any loop is equal to a positive integer multiple or zero multiple of the time step Δt (see [25], pp. 271–272).

To assure a realizable WDF ladder structure we can use constrained interconnection networks. A constrained adaptor has one input port matched. Consequently, no reflections occur at this port and the outgoing wave of the constrained port is independent of the incoming wave on that port. To

match the constrained port we need to chose appropriately the reference impedance of that port.

An example of a WDF realization of the impedance of TM_3 radiation mode is shown in Figure 5.5. Note the constrained interconnection net-

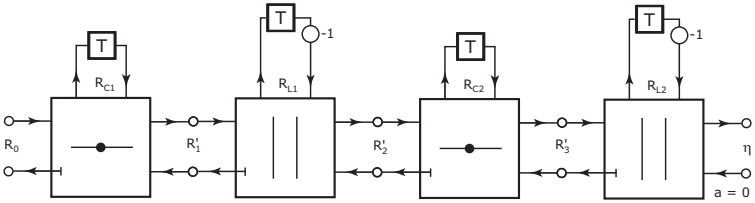

Figure 5.5: WDF ladder structure implementing the impedance of TM_3 radiation mode.

works. The constrained port is denoted by a short bar at the signal path of the outgoing wave. From the figure we can see the periodic structure of the digital filter, where the models for capacitors and inductors are alternating. This periodicity is implemented efficiently by means of a recursive algorithm.

5.3 The TLMME Algorithm

The difference between TLM and TLMME algorithms is in the application of boundary conditions. From the point of view of the TLM method the TLMME algorithm looks like a TLM algorithm with a special boundary condition[1].

The discrete time evolution is implemented in the TLM method by means of iterations. One iteration corresponds to the time evolution by one time step. The iterations are repeated for as many time steps as required. One TLM iteration is shown in Figure 5.6. We can see that the TLM itera-

[1]This is a result which we expect. Eventually, the ME is simulating a radiation boundary condition.

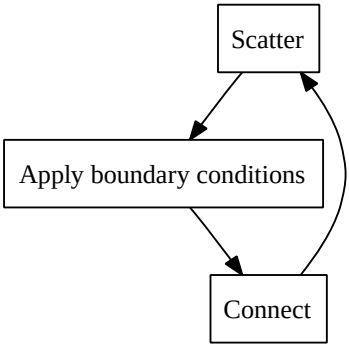

Figure 5.6: One TLM iteration – evolution by one time step.

tion begins with the scattering process – the *Scatter* procedure. The scatter procedure is applied to each TLM cell.

Next, the boundary conditions are processed – the *Apply boundary conditions* procedure. At this state of the iteration the wave quantities are located at the interfaces of the TLM cells. Inside this procedure the excitation is processed and the boundary conditions are applied.

Eventually, the wave quantities between neighbouring cells are exchanged – the *Connect* procedure – and become incoming waves for the next iteration. The iteration can start from the beginning.

The TLMME algorithm is implemented inside the Apply boundary conditions procedure and is schematically depicted in Figure 5.7.

In the first step we need to store the values of outgoing waves on the discretized spherical manifold $\mathscr{S}$ (see Figure 5.1) and outgoing waves from the WDF models of radiation modes – the *Get values on sphere* and *Get outgoing WDF* procedures.

We can summarize these waves in the vector $\mathbf{a}_{TLMME}$ defined as

$$\mathbf{a}_{TLMME} = \begin{bmatrix} \mathbf{a}_{TLM} \\ \mathbf{a}_{ME} \end{bmatrix}, \tag{5.11}$$

where the vectors $\mathbf{a}_{TLM}$ and $\mathbf{a}_{ME}$ denote the outgoing waves of the spher-

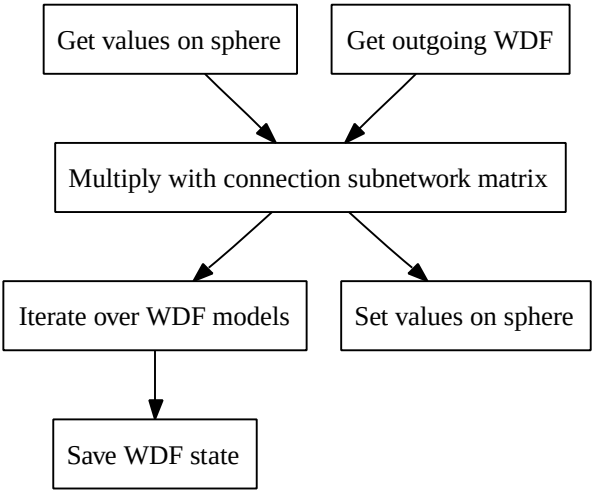

Figure 5.7: One TLMME iteration – ME boundary condition.

ical manifold and the outgoing waves from the WDF models of radiation modes, respectively. Vector $\mathbf{a}_{TLMME}$ represents the incoming waves on the connection subnetwork.

Next, we compute the outgoing waves of the connection subnetwork – the *Multiply with connection subnetwork matrix* procedure. The vector of outgoing waves from the connection subnetwork is denoted by $\mathbf{b}_{TLMME}$,

$$\mathbf{b}_{TLMME} = \begin{bmatrix} \mathbf{b}_{TLM} \\ \mathbf{b}_{ME} \end{bmatrix}. \tag{5.12}$$

The result of the Multiply with connection subnetwork matrix procedure is the vector $\mathbf{b}_{TLMME}$ calculated as

$$\mathbf{b}_{TLMME} = \mathbf{S}_{TLMME}\, \mathbf{a}_{TLMME}, \tag{5.13}$$

where $\mathbf{S}_{TLMME}$ is the scattering matrix of the connection subnetwork. There is no time delay present in this scattering process.

The incoming waves onto the spherical manifold of the TLM domain are now available in the vector $\mathbf{b}_{TLM}$ and the incoming waves onto the WDF models of the radiation modes in the vector $\mathbf{b}_{ME}$. The incoming waves $\mathbf{b}_{TLM}$ are set on the spherical manifold in the *Set values on sphere* procedure. The incoming waves $\mathbf{b}_{ME}$ are used for one time step iteration over all WDF models – the *Iterate over WDF models* procedure.

Eventually, the state of the WDF models needs to be stored in order to be used during the next TLMME iteration. This is done in the *Save WDF state* procedure.

6 Numerical Examples

6.1 Flat Dipole Antenna

The first example on which the TLMME method and it's features will be demonstrated is a flat dipole antenna. This example is simple enough to be solved to some extent analytically, but does include enough complexity to highlight important behaviour of the TLMME method. The layout of the flat dipole antenna is shown in Figure 6.1.

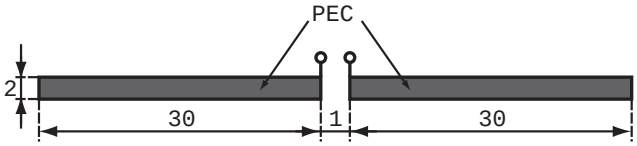

Figure 6.1: Top view of the flat dipole antenna; all lengths are given in mm units.

To evaluate the performance of the TLMME method, the input admittance of the flat dipole is chosen as the key antenna characteristics. It is well known and generally valid that the input admittance/impedance is much more sensitive to the accuracy of the modelling method than other antenna parameters like the radiation pattern (cf., e.g., [40]).

In this example the input admittance of the flat dipole is first calculated analytically. Then, a TLM computation with absorbing boundary conditions on cubical simulation region and a TLMME computation results will be presented.

6.1.1 Analytical characterization

For the analytical characterization of the flat dipole antenna an approximation by a thin wire dipole antenna is done (see [40], p. 454). The equivalent radius a_e of the wire dipole is given by

$$a_e = 0.25w, \tag{6.1}$$

where $w = 2\,\text{mm}$ is the width of the flat dipole antenna (see Figure 6.1). Using the induced emf method (see [41], pp.359–434) the real and imaginary parts of the input impedance referred to at the current maximum are given by ([40], p. 410)

$$\begin{aligned} R_m = \frac{Z_0}{2\pi}\Bigg[& C + \ln(kl) - \operatorname{Ci}(kl) + \frac{1}{2}\sin(kl)\Big(\operatorname{Si}(2kl) - 2\operatorname{Si}(kl)\Big) \\ & + \frac{1}{2}\cos(kl)\left(C + \ln\left(\frac{kl}{2}\right) + \operatorname{Ci}(2kl) - 2\operatorname{Ci}(kl)\right)\Bigg], \end{aligned} \tag{6.2a}$$

$$\begin{aligned} X_m = \frac{Z_0}{4\pi}\Bigg[& 2\operatorname{Si}(kl) + \cos(kl)(2\operatorname{Si}(kl) - \operatorname{Si}(2kl)) \\ & - \sin(kl)\left(2\operatorname{Ci}(kl) - \operatorname{Ci}(2kl) - \operatorname{Ci}\left(\frac{2ka_e^2}{l}\right)\right)\Bigg], \end{aligned} \tag{6.2b}$$

where $Z_0 = 377$, $k = \frac{\omega}{c_0}$, $C = 0.577215665$ is the Euler's constant, l is the length of the dipole, a_e is the equivalent radius of the dipole, $\operatorname{Si}(x)$ is the sine integral and $\operatorname{Ci}(x)$ is the cosine integral given by

$$\operatorname{Si}(x) = \int_0^x \frac{\sin(t)}{t}\,dt, \tag{6.3a}$$

$$\operatorname{Ci}(x) = \int_\infty^x \frac{\cos(t)}{t}\,dt. \tag{6.3b}$$

The real and imaginary parts of the input impedance referred to at the current at the input terminals are computed from

$$R_{in} = \frac{R_m}{\sin^2(kl/2)}, \tag{6.4a}$$

$$X_{in} = \frac{X_m}{\sin^2(kl/2)}. \tag{6.4b}$$

6.1.2 TLM and TLMME computations

The setup for the TLM simulation with absorbing boundary condition (ABC) and the TLMME simulation is shown in Figure 6.2. The dipole is oriented

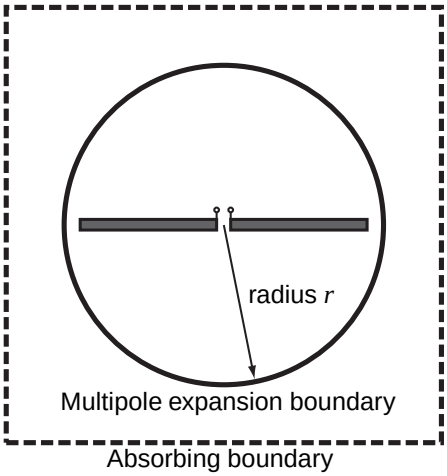

Figure 6.2: Flat dipole antenna simulation setup for TLM simulation with absorbing boundary condition and TLMME boundary condition.

along the z-axis and may be considered as rotationally symmetric. Consequently, only TM_{n0} radiation modes need to be considered. These modes have fields independent of φ.

The dipole antenna was discretized with a uniform spatial discretizetion step $\Delta x = \Delta y = \Delta z = 1\,\text{mm}$. For the TLM simulation with ABC the dimensions of the computational box are $70\,\text{mm} \times 70\,\text{mm} \times 70\,\text{mm}$ resulting in a total number of 343 000 TLM cells. For the TLMME simulation the radius $r = 35\,\text{mm}$ and the number of TM_{n0} modes $N = 5$. Both, the TLM with ABC and the TLMME simulations, were performed with $n = 5000$ time steps.

The antenna was excited with a discrete Dirac impulse on a discrete source port distributed over 2 cell interfaces. The reference resistance of the source port equals $\frac{377}{2}\,\Omega$. The 5×5 scattering matrix of the connection network reads

$$\mathbf{S} = \frac{1}{3}\begin{bmatrix} -1 & 1 & 1 & 1 & 1 \\ 2 & -2 & 1 & 1 & 1 \\ 2 & 1 & -2 & 1 & 1 \\ 2 & 1 & 1 & -2 & 1 \\ 2 & 1 & 1 & 1 & -2 \end{bmatrix}. \tag{6.5}$$

It can be verified by direct computation that this scattering matrix is energy conservative, i.e., $|\det(\mathbf{S})| = 1$, and that $\mathbf{S} \cdot \mathbf{S} = \mathbf{I}$. The matrix is not symmetric since the reference resistances on the ports differ.

The results of the calculated input admittance by the TLM and the TLMME are shown in Figure 6.3 and Figure 6.4. The results are compared with a result obtained by method of moments (MoM). The MoM computation was done using EMAP5 software [42].

We can see a good agreement between the different methods. The admittance computed by the TLMME method agrees slightly better with the MoM computation than the TLM computation with ABC.

Furthermore, in contrast to the TLM calculation with ABC, the TLMME computation provides us with novel information about the radiated field, e.g., the amount of radiated energy and the distribution of this energy among the different radiation modes. This kind of information is never available when using TLM with ABC. Also, since the temporal dependence of the modal coefficients is known in the TLMME method, we can reconstruct the radiated field without the need to re-simulate the whole problem.

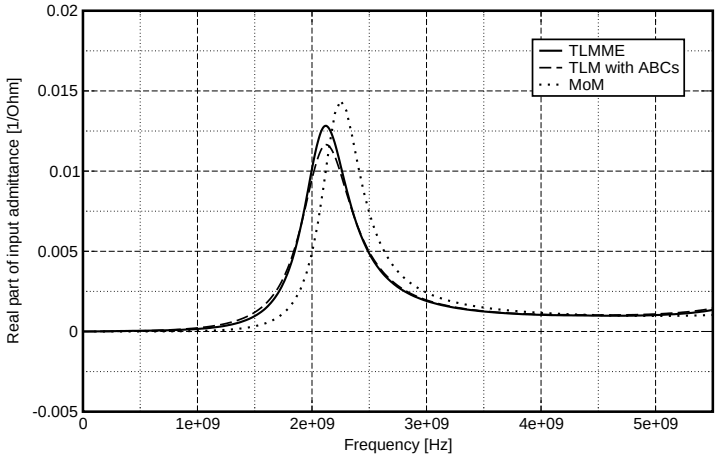

Figure 6.3: Real part of the input admittance of the flat dipole antenna.

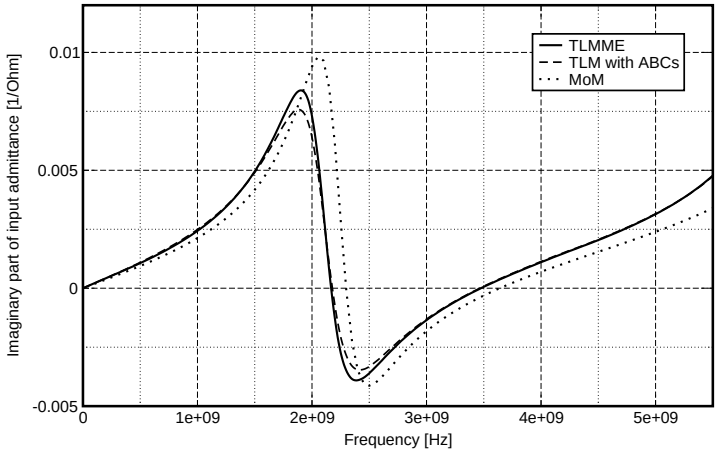

Figure 6.4: Imaginary part of the input admittance of the flat dipole antenna.

In Figure 6.5 we can see the instantaneous energy of the incoming, reflected and transmitted (radiated) signals. A detailed view on the energy of reflected signal is shown in Figure 6.6. We see that the amount of energy reflected from the radiation modes back to the TLM domain is much smaller compared to the amount of energy transmitted to the termination impedances of the radiation modes. Consequently, most of the energy is radiated. This explains why the results obtained by TLM with ABC and by TLMME are similar in this particular example.

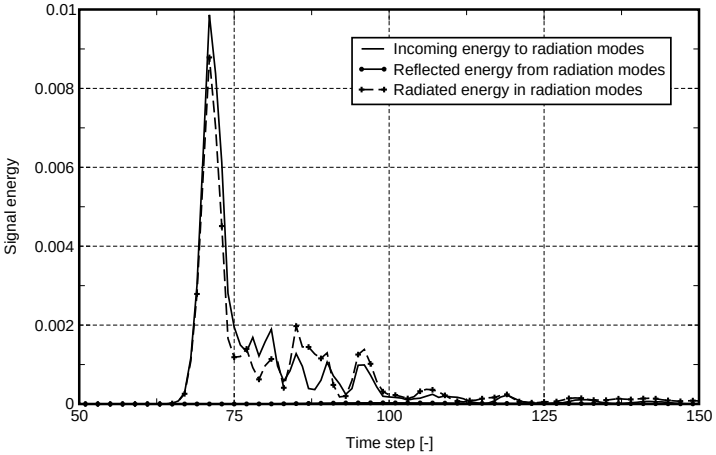

Figure 6.5: Energy of incoming, reflected and radiated signals.

6.2 Dipole Antenna at the Boundary of Simulation Region

For the absorbing boundary condition to work properly, there must be a certain distance between the geometric object and the computational boundary. In this example a dipole antenna of 6 mm length is placed at the boundary of the simulation region and its input impedance is computed.

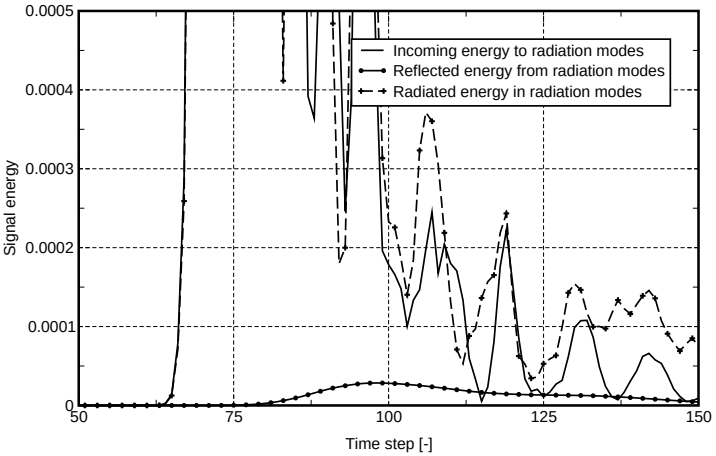

Figure 6.6: Detailed view on the energy of the reflected signal.

For the comparison the following simulation setups are used:

1. Reference simulation with ABC,
2. TLM with ABC on cubical simulation region,
3. TLM with ABC on spherical TLM region,
4. TLMME boundary condition on spherical TLM region.

The discretized dipole antenna inside the spherical TLM region is shown in Figure 6.7. Except in the case of the reference simulation, the dipole antenna is touching directly the boundary of the simulation region.

For the reference simulation a simulation domain of the size of $50\,\text{mm} \times 50\,\text{mm} \times 50\,\text{mm}$ was used. The other parameters were the same as those described below for the other simulations.

The setup for the ABC and TLMME simulations was:

- Simulation domain of $20\,\text{mm} \times 20\,\text{mm} \times 20\,\text{mm}$,

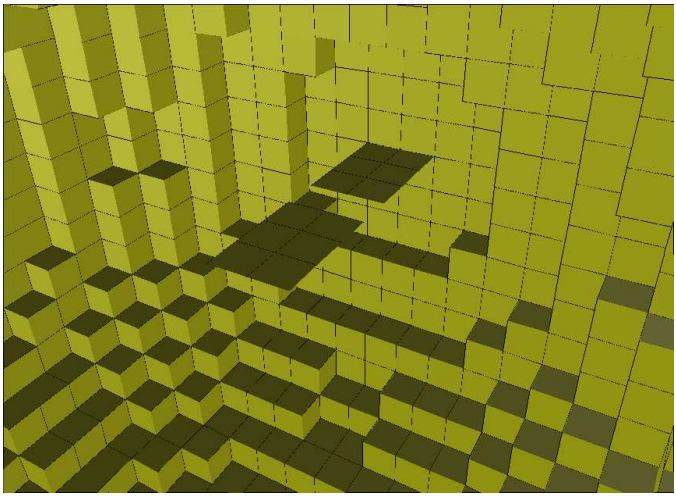

Figure 6.7: Dipole antenna inside spherical TLM region. The antenna is touching the boundary of the simulation region.

- Uniform spatial discretization with $\Delta x = \Delta y = \Delta z = 1\,\text{mm}$,
- Number of TLM iterations $n = 500$ time steps,
- Radius of the spherical TLM region $r = 10\,\text{mm}$,
- Excitation by a discrete Dirac impulse on a discrete source port distributed over 2 cells with reference port resistance equal $377/2\,\Omega$ (same as in the previous example).

For the TLMME simulation only TM_{n0} modes were considered and the number of modes was $N = 25$.

The results of the computed input impedance for the different setups are shown in Figure 6.8. We can see that the results of ABC simulations when the dipole is touching the boundary are not correct in both cases, the cubical simulation region and the spherical simulation region. The reactive

part of the input impedance does not properly reflect the resonance of the antenna. On the other hand, we can see a good agreement between the

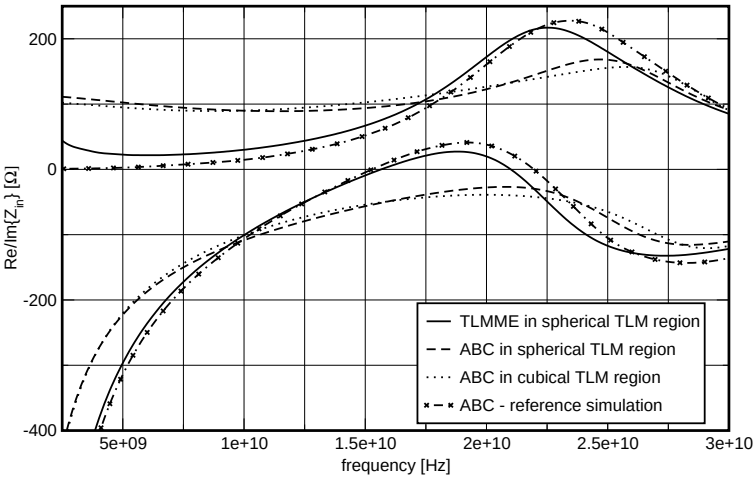

Figure 6.8: Real and imaginary parts of the input impedance of the 6 mm dipole for different simulation setups.

TLMME simulation and the reference simulation, even if the antenna is touching the boundary of the simulation region. The imaginary part reflects correctly the resonances of the antenna and also the real part agrees well with the reference simulation.

6.3 Bowtie Antenna

In this example the input impedance of broadband planar bowtie antenna is computed. The purpose of this example is to demonstrate the performance of the developed excitation techniques by means of interconnection networks (see Section 2.4).

The dimensions of the antenna structure are shown in Figure 6.9. As

was the case in the previous section, also here for the bowtie antenna the input impedance is the main antenna characteristics of interest.

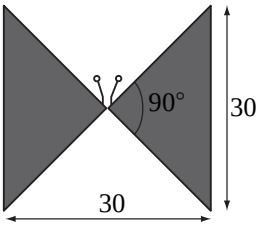

Figure 6.9: The bowtie antenna; all dimensions are given in mm.

The bowtie antenna was discretized with a spatial discretizetion step $\Delta l = 0.25\,\text{mm}$ in a computational box with dimensions $50\,\text{mm} \times 50\,\text{mm} \times 50\,\text{mm}$. At the outer boundary of the simulation domain absorbing boundary conditions were applied.

For the excitation a discrete power source with a connection network distributed across 2×2 cell interfaces was used. The antenna was excited with a Dirac impulse. The WDF representation of the connection network is shown in Figure 6.10. The port impedances of the ports were chosen so that realizability is ensured (see Section 5.2.2 and [25], pp. 271–272). The 9×9 scattering matrix of the connection network reads

$$\mathbf{S} = -\frac{1}{4}\begin{bmatrix} 0 & \mathbf{V}_1{}^T & \mathbf{V}_1{}^T \\ 2\mathbf{V}_1 & \mathbf{M}_1 & \mathbf{M}_2 \\ 2\mathbf{V}_1 & \mathbf{M}_2 & \mathbf{M}_1 \end{bmatrix}, \tag{6.6a}$$

where

$$\mathbf{V}_1 = \begin{bmatrix} 1 & 1 & 1 & 1 \end{bmatrix}^T, \tag{6.6b}$$

$$\mathbf{M}_1 = \frac{1}{2}\begin{bmatrix} 3 & -5 & 3 & 3 \\ -5 & 3 & 3 & 3 \\ 3 & 3 & 3 & -5 \\ 3 & 3 & -5 & 3 \end{bmatrix} \tag{6.6c}$$

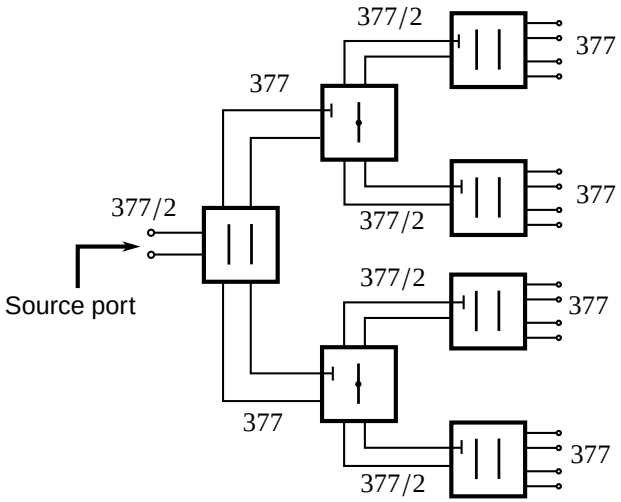

Figure 6.10: WDF representation of a 2×2 connection network; the port impedances are also shown.

and

$$\mathbf{M}_2 = -\frac{1}{2}\begin{bmatrix} 1 & 1 & 1 & 1 \\ 1 & 1 & 1 & 1 \\ 1 & 1 & 1 & 1 \\ 1 & 1 & 1 & 1 \end{bmatrix}. \tag{6.6d}$$

It can be checked by direct computation that $\mathbf{S} \cdot \mathbf{S} = \mathbf{I}$ and $|\det(\mathbf{S})| = 1$.

The result of the computed input impedance using the discrete source in TLM is shown in Figure 6.11. We can see a good agreement with method of moments (MoM) result presented in [43] and measurement result presented in [44].

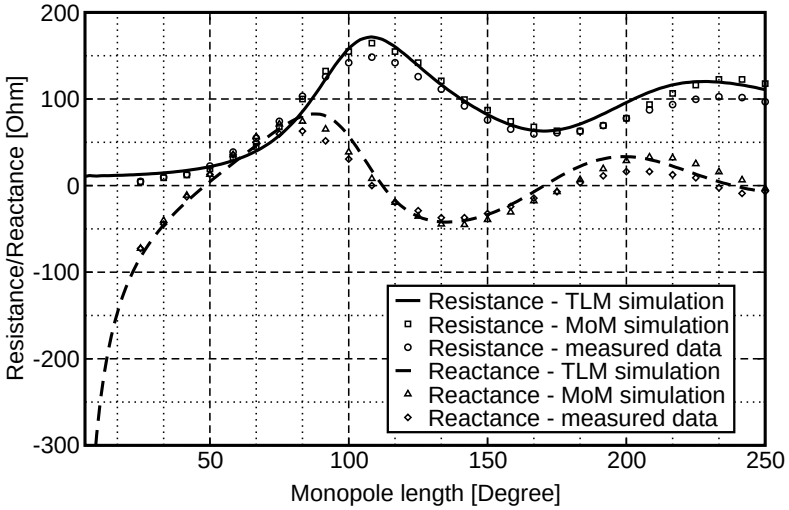

Figure 6.11: Input impedance of the bowtie antenna. MoM simulation results are taken from [43] and measurement results from [44].

In Figure 6.12 the first 150 time steps of the reflected wave at the source port are shown. From the returns to zero of the signal can be clearly seen that non-physical modes are present in the simulation. However, since the

TLM model is linear and since there is only one source port, the results for low frequency components are correct.

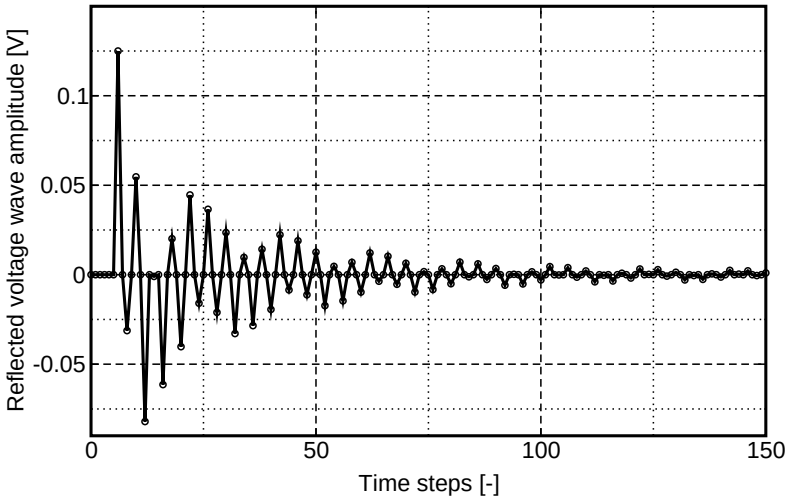

Figure 6.12: Time domain signal for 150 time steps of the reflected wave at the source port.

7 Conclusions

In this thesis the Transmission Line Matrix — Multipole Expansion method (TLMME) has been presented. The TLMME method allows an efficient and potentially exact modeling of radiating electromagnetic structures.

In TLMME the time-domain Transmission Line Matrix (TLM) method is combined with the multipole expansion of the radiated field. The total radiated field is decomposed into orthonormal radiation modes which are connected to the TLM simulation domain on a spherical boundary. In a global network model the simulation domain is modeled by the TLM mesh of transmission lines, every impedance of the radiation mode is modeled by a ladder network oneport and the connection of these partial networks is accomplished by an ideal transformer connection network. This allows to include potentially exact radiating boundary condition into the TLM model by lumped element equivalent circuits representing the impedances of radiation modes.

In Chapter 2 the principles of the TLM method were introduced. It was shown how the scattering matrix of the TLM method is obtained using discrete differential forms. Furthermore, novel techniques for the excitation of TLM cells by means of discrete sources were developed. The connection networks employed provide as port signals incoming and outgoing waves and are thus easily coupled to the TLM method which uses wave quantities as well. Also, they enable the excitation of the TLM model with a discrete Dirac impulse signal. Very good performance of the discrete excitation technique was verified on an example of bowtie antenna in Section 6.3.

In Chapter 3 the theory of multipole expansion and radiation modes was given. It was shown how the impedances of radiation modes can be represented using equivalent Cauer circuits.

In Chapter 4 the connection subnetwork connecting the TLM region to the impedances of the radiation modes was described. The scattering ma-

trix of the connection subnetwork was derived and its special cases were discussed.

The TLMME method was described in detail in Chapter 5. The spherical TLM region was described and its generation by means of Cartesian mesh generator was explained. The performance of the Cartesian mesh generator was evaluated on an example of a rectangular cavity resonator. We could calculate the resonance frequencies with a relative error below 0.2 % for the highest mesh resolution. Furthermore, the realizations of the impedances of the radiation modes by means of wave digital filters (WDFs) were described and the details of the TLMME algorithm were explained in detail.

The results of the calculation of the input impedance of antennas using the TLMME method were given in Chapter 6. First, a flat dipole antenna was characterized. We have seen good agreement between the results obtained by the TLMME method, the TLM method using absorbing boundary condition (ABC) and the method of moments (MoM). However, in contrast to the TLM method with ABC, the availability of additional information about the radiated field in the TLMME method could explain why the solution using TLM with ABC is similar to that of TLMME for the particular example. For the example of the flat dipole antenna most of the field hitting the boundary of the simulation domain is radiated, as could be observed from the energy transmitted to the termination impedances of the radiation modes.

In the example of a dipole antenna located at the boundary of the simulation domain was shown that the TLMME method gives better result of the input impedance of the antenna than the TLM method with ABC. In contrast to the TLM method with ABC the input impedance computed by the TLMME method was correct even if the dipole antenna is touching the boundary of the simulation domain.

There still remain many tasks which could be done in the future. One problem of the TLMME method in the current implementation is the nonconformity of the discretized spherical manifold to the true spherical manifold. When a tetrahedral implementation of TLM is available, the performance of the TLMME method could be tested with a spherical TLM simulation region conforming better to the true spherical manifold.

Furthermore, planar structures with conducting ground are a set of very important problems in today's industry. To solve the radiation problems of these planar structures efficiently by TLMME, a half-space formulation of the TLMME could be developed and implemented.

A Useful Formulas and Relations

A.1 Central Difference Scheme

Let's have a function $f(x)$ of $x \in \mathbb{R}$ and $f : \mathbb{R} \to \mathbb{R}$. The first central difference, using discretization step Δx, is given by

$$\left[\frac{\mathrm{d}f(x)}{\mathrm{d}x}\right]_D = \frac{\Delta f(x)}{\Delta x} = \frac{f(x+\frac{\Delta x}{2}) - f(x-\frac{\Delta x}{2})}{\Delta x} = f'_\Delta(x). \tag{A.1}$$

The second order central difference is then obtained by

$$\begin{aligned}\left[\frac{\mathrm{d}^2 f(x)}{\mathrm{d}x^2}\right]_D &= \left[\frac{\mathrm{d}}{\mathrm{d}x}\left(\left[\frac{\mathrm{d}f(x)}{\mathrm{d}x}\right]_D\right)\right]_D = \left[\frac{\mathrm{d}}{\mathrm{d}x}\left(\frac{\Delta f(x)}{\Delta x}\right)\right]_D = \left[\frac{\mathrm{d}}{\mathrm{d}x} f'_\Delta(x)\right]_D = \\ &= \frac{f'_\Delta(x+\frac{\Delta x}{2}) - f'_\Delta(x-\frac{\Delta x}{2})}{\Delta x} = \\ &= \frac{1}{\Delta x^2}(f(x+\Delta x) - 2f(x) + f(x-\Delta x)) = \\ &= f''_\Delta(x)\end{aligned} \tag{A.2}$$

A.2 Transformations Between Wave and Network Quantities

Possible transformations from network quantities to wave quantities $\mathbf{T}_W$ and from wave quantities to network quantities $\mathbf{T}_N$.

Transformation 1

$$\mathbf{T}_W = \frac{1}{\sqrt{2}}\begin{bmatrix} 1 & \eta \\ 1 & -\eta \end{bmatrix} \tag{A.3a}$$

$$\mathbf{T}_N = \frac{1}{\sqrt{2}}\begin{bmatrix} 1 & 1 \\ \frac{1}{\eta} & -\frac{1}{\eta} \end{bmatrix} \tag{A.3b}$$

Transformation 2

$$\mathbf{T}_W = \begin{bmatrix} 1 & \eta \\ 1 & -\eta \end{bmatrix} \tag{A.4a}$$

$$\mathbf{T}_N = \frac{1}{2}\begin{bmatrix} 1 & 1 \\ \frac{1}{\eta} & -\frac{1}{\eta} \end{bmatrix} \tag{A.4b}$$

Transformation 3

$$\mathbf{T}_W = \frac{1}{2}\begin{bmatrix} 1 & \eta \\ 1 & -\eta \end{bmatrix} \tag{A.5a}$$

$$\mathbf{T}_N = \begin{bmatrix} 1 & 1 \\ \frac{1}{\eta} & -\frac{1}{\eta} \end{bmatrix} \tag{A.5b}$$

Normalized wave quantities

$$V' = \frac{V}{\sqrt{\eta}}, \qquad I' = I\sqrt{\eta} \tag{A.6}$$

$$z = \frac{V'}{I'} = \frac{1}{\eta}\frac{V}{I} = \frac{Z}{\eta} \tag{A.7}$$

Then, transformation 1 reads

$$\mathbf{T}_W = \frac{1}{\sqrt{2}}\begin{bmatrix} 1 & 1 \\ 1 & -1 \end{bmatrix} \tag{A.8a}$$

$$\mathbf{T}_N = \frac{1}{\sqrt{2}}\begin{bmatrix} 1 & 1 \\ 1 & -1 \end{bmatrix} = \mathbf{T}_W \tag{A.8b}$$

A.3 Matrix Algebra Rules

A.3.1 Transposition and inversion

$$(\mathbf{A}^T)^T = \mathbf{A} \tag{A.9}$$

$$(\mathbf{A} \pm \mathbf{B})^T = \mathbf{A}^T \pm \mathbf{B}^T \tag{A.10}$$

$$(\mathbf{AB})^T = \mathbf{B}^T\mathbf{A}^T \tag{A.11}$$

$$(\mathbf{ABC})^T = (\mathbf{BC})^T\mathbf{A}^T = \mathbf{C}^T\mathbf{B}^T\mathbf{A}^T \tag{A.12}$$

For any nonsingular matrix $\mathbf{A}$

$$(\mathbf{A}^T)^{-1} = (\mathbf{A}^{-1})^T \tag{A.13}$$

A.3.2 Block matrix and Schur complement

In the following consider the matrices $[\mathbf{A}]_{p\times p}$, $[\mathbf{B}]_{p\times q}$, $[\mathbf{C}]_{q\times p}$, $[\mathbf{D}]_{q\times q}$, where $\mathbf{D}$ is nonsingular. Let $[\mathbf{M}]_{(p+q)\times(p+q)}$ be the block matrix (partitioned matrix)

$$\mathbf{M} = \begin{bmatrix} \mathbf{A} & \mathbf{B} \\ \mathbf{C} & \mathbf{D} \end{bmatrix}. \tag{A.14}$$

The transpose of $\mathbf{M}$ is given by

$$\mathbf{M}^T = \begin{bmatrix} \mathbf{A} & \mathbf{B} \\ \mathbf{C} & \mathbf{D} \end{bmatrix}^T = \begin{bmatrix} \mathbf{A}^T & \mathbf{C}^T \\ \mathbf{B}^T & \mathbf{D}^T \end{bmatrix}. \tag{A.15}$$

The Schur complement $\mathbf{S}_A$ is defined as

$$\mathbf{S}_A = \mathbf{A} - \mathbf{B}\mathbf{D}^{-1}\mathbf{C}. \tag{A.16}$$

With the Schur complement the inverse matrix $\mathbf{M}^{-1}$ can be calculated as

$$\begin{bmatrix} \mathbf{A} & \mathbf{B} \\ \mathbf{C} & \mathbf{D} \end{bmatrix}^{-1} = \begin{bmatrix} \mathbf{I} & \mathbf{0} \\ -\mathbf{D}^{-1}\mathbf{C} & \mathbf{I} \end{bmatrix} \begin{bmatrix} \mathbf{S}_A^{-1} & \mathbf{0} \\ \mathbf{0} & \mathbf{D}^{-1} \end{bmatrix} \begin{bmatrix} \mathbf{I} & -\mathbf{B}\mathbf{D}^{-1} \\ \mathbf{0} & \mathbf{I} \end{bmatrix}. \tag{A.17}$$

A.4 Taylor Expansion in 2D

The Taylor expansion of a two-dimensional function $f(x+\Delta x, y+\Delta y)$ around the point (x,y) is given by

$$f(x+\Delta x, y+\Delta y) = f(x,y) + \Big((\Delta x) f_x + (\Delta y) f_y\Big) + \\ + \frac{1}{2}\Big((\Delta x)^2 f_{xx} + 2\Delta x \Delta y f_{xy} + (\Delta y)^2 f_{yy}\Big) + \ldots, \tag{A.18}$$

with $f_x = \partial f(x,y)/\partial x$, $f_{xx} = \partial^2 f(x,y)/\partial x^2$, etc.

Bibliography

[1] Peter Russer, Mauro Mongiardo, and Leopold B. Felsen. Electromagnetic field representations and computations in complex structures III: network representations of the connection and subdomain circuits. *Int. J. Numerical Modelling*, 15(1):127–145, January 2002.

[2] P. B. Johns and R. L. Beurle. Numerical solution of 2-dimensional scattering problems using a transmission-line matrix. *Proc. Inst. Elec. Eng.*, 118:1203–1208, September 1971.

[3] W.J.R. Hoefer. The transmission line matrix method-theory and applications. *IEEE Trans. Microwave Theory Techn.*, 33(10):882–893, October 1985.

[4] B. Engquist and A. Majda. Absorbing boundary conditions for numerical simulation of waves. *PNAS*, 74(5):1765–1766, May 1977.

[5] J. P. Berenger. A perfectly matched layer for the absorption of electromagnetic waves. *J. Comp. Phy.*, pages 185–200, October 1994.

[6] J. A. Morente, J. A. Porti, and M. Khalladi. Absorbing boundary conditions for the TLM method. *IEEE Trans. Microwave Theory Tech.*, pages 2095–2099, November 1992.

[7] C. Eswarappa and W. J. R. Hoefer. Implementation of Berenger absorbing boundary conditions in TLM by interfacing FDTD perfectly matched layers. *Electronics Letters*, 31:1264–1266, July 1995.

[8] N. Peña and M. M. Ney. Absorbing-boundary conditions using perfectly matched-layer (PML) technique for three-dimensional TLM simulations. *IEEE Trans. Microwave Theory Tech.*, pages 1749–1755, October 1997.

[9] J. L. Dubard and D. Pompei. Simulation of Berenger's perfectly matched layer with a modified TLM node. *IEE Proc. Microwaves, Antennas, Propagat.*, 144:205–207, June 1997.

[10] P. Russer. Network-oriented modeling of radiating electromagnetic structures. *Turk. J. Elec. Engin.*, 10(2):147–162, 2002.

[11] P. Russer. *Electromagnetics, Microwave Circuit and Antenna Design for Communications Engineering*. Artech House, Inc., Boston, second edition, 2006.

[12] P.B. Johns and R.L. Beurle. Numerical solution of 2-dimensional scattering problems using a transmission-line matrix. *Proc. IEE*, 118(9):1203–1208, September 1971.

[13] P. B. Johns. A symmetrical condensed node for the TLM method. *IEEE Trans. Microwave Theory Tech.*, MTT-35(4), April 1987.

[14] Z. Chen, M. M. Ney, and W. J. R. Hoefer. A new finite-difference time-domain formulation and its equivalence with the TLM symmetrical condensed node. *IEEE Trans. Microwave Theory Techn.*, 39(12):2160–2169, December 1991.

[15] S. Hein. Consistent finite difference modelling of Maxwell's equations with lossy symmetrical condensed TLM node. *Int. J. Numer. Modeling*, 6:207–220, 1993.

[16] M. Krumpholz and P. Russer. A field theoretical derivation TLM. *IEEE Trans. Microwave Theory Techn.*, 42(9):1660–1668, September 1994.

[17] M. Krumpholz, P. Russer, Q. Zhang, and W.J.R. Hoefer. Field-theoretic foundation of two-dimensional TLM based on a rectangular mesh. *1994 Int. Microwave Symposium Digest, San Diego*, pages 333–336, May 1994.

[18] H. Jin and R. Vahldieck. Direct derivations of TLM symmetrical condensed node and hybrid symmetrical condensed node from maxwell's

equations using centered differencing and averaging. *IEEE Trans. Microwave Theory Techn.*, 42(12):2554–2561, December 1994.

[19] V. Trenkic, C. Christopoulos, and T. Benson. Theory of the symmetrical super-condensed node for the TLM method, 1995.

[20] T. Toffoli. Cellular automata as an alternative to (rather than an approximation of) differential equations in modeling physics. *Physica D Nonlinear Phenomena*, 10:117–127, January 1984.

[21] Tommaso Toffoli. *Cellular Automata Machines: A new environment for modeling*. The MIT Press, 1987.

[22] K. Kaneko. Simulating physics with coupled map lattices—pattern dynamics, information flow, and thermodynamics of spatiotemporal chaos. *Formation, Dynamics and Statistics of Patterns*, 1:1–54, 1990.

[23] M. J. Harris, G. Coombe, T. Scheuermann, and A. Lastra. Physically-based visual simulation on graphics hardware. In *HWWS '02: Proceedings of the ACM SIGGRAPH/EUROGRAPHICS conference on Graphics hardware*, pages 109–118, Aire-la-Ville, Switzerland, Switzerland, 2002. Eurographics Association.

[24] James P. Sethna. *Statistical Mechanics: Entropy, Order Parameters, and Complexity*. Oxford University Press, 2006.

[25] A. Fettweis. Wave digital filters: Theory and practice. *Proc. IEEE*, 74(2):270–327, Feb. 1986.

[26] C. Christopoulos. *The Transmission-Line Modeling Method TLM*. New York: IEEE Press, 1995.

[27] A. N. Hirani. *Discrete Exterior Calculus*. Ph.d dissertation, California Institute of Technology, U.S.A., May 2003.

[28] L. B. Felsen and N. Marcuvitz. *Radiation and Scattering of Waves*. IEEE Press, 445 Hoes Lane, PO Box 1331, Piscataway, NJ 08855-1331, second edition, 1994.

[29] K. F. Warnick, R. Selfridge, and D. Arnold. Electromagnetic boundary conditions and differential forms. volume 142, pages 326–332, August 1995.

[30] M. Abramowitz and I. A. Stegun. *Handbook of Mathematical Functions*. Dover Publications, Inc., New York, fifth edition, 1968.

[31] L. J. Chu. Physical limitations of omni-directional antennas. *J. Applied Physics*, pages 1163–1175, December 1948.

[32] B.D.H. Tellegen. A general network theorem with applications. *Proc. Inst. Radio Engineers*, 14:265–270, 1953.

[33] P. Penfield, R. Spence, and S. Duinker. *Tellegen's theorem and electrical networks*. MIT Press, Cambridge, Massachusetts, 1970.

[34] G. C. Temes. A physical proof of Tellegen's theorem. In *Proceedings of the IEEE*, volume 57, pages 1183–1184, June 1969.

[35] K. C. Gupta, Ramesh Garg, and Rakesh Chadha. *Computer-Aided Design of Microwave Circuits*. Artech House, 1981.

[36] Y. Srisukh, J. Nehrbass, F. L. Teixeira, J. F. Lee, and R. Lee. An approach for automatic Grid generation in three-dimensional FDTD simulations of complex geometries. *IEEE Antennas and Propagation Magazine*, 44(4):75–80, August 2002.

[37] P. Sewell, J. G. Wykes, T. M. Benson, C. Christopoulos, D. W. P. Thomas, and A. Vukovic. Transmission-line modeling using unstructured triangular meshes. *IEEE Trans. Microwave Theory Tech.*, 52(5):1490–1497, May 2004.

[38] A. C. Cangellaris and D. B. Wright. Analysis of the numerical error caused by the stair-stepped approximation of a conducting boundary in FDTD simulations of electromagnetic phenomena. *IEEE Trans. Antennas and Prop.*, 39(10):1518–1525, October 1991.

[39] Y. S. Rickard and N. K. Nikolova. Off-grid perfect boundary conditions for the FDTD method. *IEEE Trans. Microwave Theory Techn.*, 53(7):2274–2283, July 2005.

[40] Constantine A. Balanis. *Antenna Theory*. John Wiley & Sons, Inc., second edition, 1997.

[41] John D. Kraus. *Antennas*. McGraw Hill, New York, 1988.

[42] EMAP5 software package (http://www.emclab.umr.edu/emap5/).

[43] C. J. Leat, N. V. Shuley, and G. F. Stickley. Triangular-patch model of bowtie antennas: validation against Brown and Woodward. *IEE Proc.-Microw. Antennas Propag.*, 145(6):465–470, Dec. 1998.

[44] G. H. Brown and O. M. Woodward. Experimentally determined radiation characteristics of conical and triangular antennas. *RCA Rev.*, 13:425–452, Dec. 1952.